

INTERNATIONAL JOURNAL OF
Peening Science and Technology

EDITOR-IN-CHIEF

PRATIK SHUKLA

- Preface** 181
Pratik Shukla
- Characterization of Laser Ultrasonic in Ablation Regime Using Filter and Hilbert Transform** 183
D. Mangaiyarkarasi, Vinuthashri, T. Zhenkui, K. O. Y. Keng, C. Long, S. H. Wei, S. Yali, C. Lianwei and M. Hong
- Investigation on High Power Laser Removal of Thermal Barrier Coating (TBC) and Bond Layer (MCrAlY) from Inconel 718 Alloy** 201
J. C. Hernandez-Castaneda, W. Y. Chi, F. Yongwei, N. F. Lan, M. C. C. Khin and Z. Hongyu
- Evaluation of Surface Properties of Silicon Nitride Ceramics Treated with Laser Peening** 221
K. Saigusa, K. Takahashi and N. Sibuya
- Estimation of Laser Shock Peening Induced Plastic Deformation in Hastelloy-X Superalloys** 233
S. Nath, P. Shukla, X. Shen, A. Behera and J. Lawrence

o c p s c i e n c e

INTERNATIONAL JOURNAL OF

Peening Science and Technology

(Print) ISSN 2473-506X • (Online) ISSN 2473-5078

PAPERS IN THIS JOURNAL ARE AVAILABLE
ON-LINE BEFORE THE PRINT COPY
www.oldcitypublishing.com/journals/JPST-home/

Volume 1, Number 3, 2019

International Journal of Peening Science and Technology

Pages 181-258

International Journal of Peening Science and Technology (IJPST)

EDITOR-IN-CHIEF

Pratik Shukla

School of Mechanical, Aerospace and Automotive Engineering, Faculty of Engineering, Environment and Computing, Coventry University, Priory Street, Coventry, CV1 5FB, United Kingdom

E-mail: ijpst@oldcitypublishing.com

Web: <https://www.pratikshukla.com/>

EDITORIAL BOARD

Ric Allot, STFC Rutherfordford Appleton Laboratory, Harwell Science and Innovation Campus, UK • **Auezhan Amanov**, Institute for Manufacturing System Technology, Sun Moon University, South Korea • **Laurent Berthe**, CNRS – Labo PIMM, France • **Supriyo Ganguly**, Welding Engineering and Laser Processing Centre, Cranfield University, UK • **Ramana Grandhi**, College of Engineering and Computer Science, Wright State University, USA • **Janez Grum**, Faculty of Mechanical Engineering, University of Ljubljana, Slovenia • **Kiran Gulia**, School of Metallurgy and Materials, University of Birmingham, UK • **Lloyd Hackel**, Metal Improvement Company, Curtiss-Wright Surface Technologies, USA • **S. Kalainathan**, School of Advanced Sciences, VIT University, India • **Lin Li**, School of Mechanical, Aerospace and Civil Engineering, University of Manchester, UK • **Jyotsna Dutta Majumdar**, Department of Metallurgical & Materials Engineering, Indian Institute of Technology, Kharagpur, India • **Sundar Marimuthu**, The Manufacturing Technology Centre (MTC), UK • **Jino Mathews**, Faculty of Engineering, Environment and Computing, Coventry University, Coventry, UK • **C P Paul**, Head, Laser Additive Manufacturing Laboratory, Raja Ramanna Centre for Advanced Technology, India • **Claudia Polese**, School of Mechanical, Industrial and Aeronautical Engineering, University of the Witwatersrand, South Africa • **Yuji Sano**, ImpACT (Impulsing Paradigm Change through Disruptive Technologies), Japan Science and Technology Agency, Japan • **Niall Smyth**, Faculty of Engineering, Environment and Computing, Coventry University, UK • **Phil Swanson**, Faculty of Engineering, Environment and Computing, Coventry University, UK • **Abhishek Telang**, Research and Development, Cardio and Vascular Division, Integer (Lake Region Medical), Minnesota, USA • **Vijay Vasudevan**, Department of Mechanical and Materials Engineering, University of Cincinnati, USA • **Houzheng Wu**, Department of Materials, Loughborough University, UK • **Ann Zammit**, Department of Metallurgy and Materials Engineering, University of Malta, Malta

Aims and Scope:

The *International Journal of Peening Science and Technology (IJPST)* aims to provide a global and multidisciplinary forum for the exchange of the science, technology, developments and applications surrounding the wide variety of peening techniques available. The Journal highlights the latest development which peening technologies have made to provide both scientific and industrial progress. Emphasis is placed on both the theoretical and practical contributions in relation to the methods, technologies, new applications/materials, and evaluates results and developments of enhanced solutions, new experimental methods and associated phenomena. Original research papers, case studies, review papers, short communications, mini reviews and letters to editor are all welcome. The scope of the journal is defined to include but, not limited to, the following areas: laser shock peening (LSP); plasma physics and dynamics; grit blasting; shot peening; blast and laser cleaning; ultrasonic peening; water-jet/cavitation peening; oil-jet peening; ion exchange beam peening; low plasticity burnishing and deep rolling; other material strengthening treatments; issues on plastic deformation and strengthening mechanisms; residual stresses and its management in materials; finite element analysis (FEA) and process modelling of the peening techniques; topographical and micro and nano structural characteristics; change in mechanical, electrical and biomedical properties using such peening techniques and reflects the main areas in which peening methods are used and developed for the surface engineering and for manufacturing applications.

Papers submitted for publication must be in English and must follow a prescribed format. All papers will be subjected to a critical peer-review prior to publication. Notes for contributors can be found at the back of the journal.

© 2019 Old City Publishing, Inc. Published by license under the OCP Science imprint, a member of the Old City Publishing Group. All rights reserved.

Except as permitted under national laws or under the photocopy license described below, no part of this publication may be reproduced or transmitted in any form or by any means, electronic, mechanical, photocopying or otherwise, or stored in a retrieval system of any nature, without the advance written permission of the Publisher.

Publisher's World Wide Web Address

Additional information is available through the Publisher's web site at:
<http://www.oldcitypublishing.com>.

Ordering Information

Four issues per volume. Subscriptions are renewed on an annual basis. 2019 Volume: 1. Orders may be placed with your usual supplier or at the address shown below. Journal subscriptions are sold on a per volume basis only; single issues of the current volume are not available separately. Claims for non-receipt of issues will be honored if made within three months of publication of the issue. All issues are dispatched by airmail throughout the world.

Subscription Rates

Institutional rate (includes print and on-line): US \$1080 EURO €967 ¥122,600

Individual rate (includes print version only): US \$215 EURO €205 ¥26,340

The individual rate is available only to individuals whose library subscribes to the journal OR who warrant that the journal is for their own personal use. Orders must be sent directly to the Publisher and payment must be made by personal check or credit card.

Publication Schedule Information

To ensure your collection is up-to-date, please call +1 215 925 4390 for information about the latest issue published or visit the publisher's web site:
<http://www.oldcitypublishing.com>.

Orders should be placed through:

Customer Services Department
Old City Publishing
628 North 2nd Street
Philadelphia, PA 19123, USA

Tel: +1 215 925 4390

Fax: +1 215 925 4371

Enquiries can also be sent by e-mail via a link on the publishers web site:

<http://www.oldcitypublishing.com>.

Rights and Permissions/Reprints of Individual Articles

This publication and each of the articles contained herein are protected by copyright.

Permission to reproduce and/or translate material contained in this journal must be obtained in writing from the Publisher.

For permission to photocopy for internal use within your organisation, or to make copies for external or academic use please contact the Copyright Clearance Center at 222 Rosewood Drive, Danvers, MA 01923, USA

Telephone: +1 978-750-8400 or online at <http://www.copyright.com/>.

Any unauthorized reproduction, transmission or storage may result in civil or criminal liability.

Printed in USA.

SEPTEMBER 2019

Preface

Here with, presents the third issue of the *International Journal of Peening Science and Technology*. This issue propagates new knowledge to academia and industry related to the science and fundamental theory of peening science and the different strengthening techniques available for engineering materials. This is a great privilege for me and it also bring me a great pleasure, because this new journal to cover these specific topics is not only important, but acts as a dedicated platform to foster collaboration and extend interest in these areas ensuring the advancement of the field.

It was necessary to specifically introduce this issue and the content within it as some of the papers published herein were very briefly presented at the 7th International Conference on Laser Peening and Related Phenomena (LSP2018), hosted at the campus of the National University of Singapore and jointly organised by Coventry University, UK on 17th to 22nd June 2018.

These papers fit into the wider scope of the journal and were peer-reviewed by at least two or more referees to ensure the work being published is novel and rigorous. I would firstly like to thanks the authors for taking the time to submit theses extended papers. The first paper demonstrates the property of different frequency distributions of the bulk and ultrasonic surface waves and applies filtering functions together with Hilbert transform, which gives instantaneous frequency and amplitude in order to separate and extract the detailed features of the ultrasound signal. These findings can be useful to investigate defects and monitor thickness of offshore structures in real-time.

The second paper reported on a new two-stage laser removal process of thermal barrier coating and bond layer of an aero engine components as an alternative to a conventional chemical bath process. Further implementation will result to safer and greener environmental conditions.

The third paper presents laser shock peening of a silicon nitride ceramic and evaluated preliminary findings of a brittle material that is usually unconventional since ceramics are hard brittle and comprise of low ductility. This paper has the potential to advance further work in this line of research.

The fourth paper (although not presented at the LSP2018) was invited and is focused on the strengthening a new Hastelloy-X, superalloys with the use

of laser shock peening. This work is presented in significant detail, potentially contributing to the application of Hastelloy-X in a gas turbine environment as well as in high temperature gas cooled reactors where cyclic loads are prevalent.

I sincerely hope these papers aid and inspire researchers to undertake further work on these topics and act as a fruitful read to enhance and update knowledge, and lastly, encourage researchers to continue their contributions to the journal.

Dr Pratik Shukla
Coventry University, U.K.

Characterization of Laser Ultrasonic in Ablation Regime Using Filter and Hilbert Transform

D. MANGAIYARKARASI, VINUTHASHRI, T. ZHENKUI,
K. O. Y. KENG, C. LONG, S. H. WEI, S. YALI,
C. LIANWEI AND M. HONG*

*National University of Singapore, Engineering Faculty, Electrical and Computer Engineering
Department, Optical Science and Engineering Centre, E6-03-03, 5 Engineering Drive 1,
Singapore 117608*

Laser generated ultrasound in ablation regime provides a large enhancement of longitudinal mode signal which is useful to investigate defects and monitor thickness of offshore structures in real time. However, the simultaneous generation of bulk and surface acoustic waves (SAW) create complexities in the detection of appropriate type of ultrasonic wave. This is due to strong surface waves, which propagate along the surface interface regions interfering with the reflected longitudinal mode signals from the defects as well as from the rear substrate surface. Thus, the signal is mostly overlapped or hidden in the tail of the surface waves detected causing the determination of the arrival time of the ultrasound a challenging one. This paper utilizes the property of different frequency distributions of the bulk and surface waves and applies filtering functions together with Hilbert transform (HT), which gives instantaneous frequency and amplitude in order to separate and extract the detailed features of the ultrasound signal. A single, distinct, unipolar waveform (positive peak) obtained with bandpass filter followed by HT combination enhances the signal amplitude which is essential for B and C scans in the laser ultrasonics where the threshold voltages are set by the positive peak voltages.

Keywords: Laser ultrasonics, ablation, plasma physics, pulsed laser, signal processing, hilbert transform, surface acoustics waves

Corresponding author's e-mail: elehmfh@nus.edu.sg

1 INTRODUCTION

1.1 Laser Ultrasonics

Non-destructive testing and evaluation (NDT&E) together with structural health monitoring (SHM) are two most common approaches used in structural investigations of materials with the advantage of real-time detection to forecast the remaining life cycles of structures and to reduce maintenance costs and time [1]. Ultrasound detection has been implemented as a NDE tool in various areas, including thickness measurements and defect detection for many decades [2]. The problems using conventional piezoelectric transducers are the need to use a coupling medium, limited bandwidth, limitation of operational use at elevated temperatures and the requirement of proper orientations of the phase sensitive piezoelectric transducer for contoured structures. These limitations can be overcome by laser ultrasonics which has the flexibility in generating ultrasound over a wide range of frequencies, transmitting and receiving ultrasound without a coupling medium, the ability to operate in harsh environmental conditions and the detection of specimens with complex geometry [3-7]. Furthermore, the laser source can be focused to the microns scale, at a much higher spatial resolution than the conventional ultrasonic beam source (size at mm scale). Meanwhile, the laser beam can raster over the sample surfaces at a high speed (dozens of mm per second) to increase the NDT throughput. Laser ultrasonics detection is reliable in real industrial situations and presently used for major industrial applications such as wafer inspection, inspection of composite components in aircrafts and wall thickness measurement of seamless steel tubes [8-9].

1.2 Generation of ultrasound with a pulsed laser

When the test sample is irradiated with a short laser pulse (ns or ps) at high energy (mJ), light energy is absorbed strongly by the electrons of the material and transferred to the lattice. Depending on the energy density, it either leads to only a temperature rise (creating thermal waves in the thermoelastic regime) or melting, vaporization and then plasma generation in the ablation regime (producing shock waves) [10, 11]. At a laser density of $< 10^7$ W/cm², the thermoelastic mechanism occurs on the metal surfaces. The absorbed laser energy produces thermal expansion and contraction resulting in the production of elastic waves. For the emission of ultrasound along normal to the surface, the penetration of laser beam should be deeper, and the diameter of the beam should be comparable to the wavelength of the ultrasound. However, when the power density increases above 10^7 W/cm², in addition to a thermoelastic expansion, the sample surface would melt and material is then ablated to create a pit of a few microns deep. The ejected material and the surrounding air are ionised by various physical process, producing plasma plume and the resulting momentum by the recoiling effect of the outward ejected materials in addition to the plasma pressure produces a point force

normal to the surface, which then enhances the amplitude of the ultrasound. In addition to these regimes, there is also a constrained surface source regime that occurs at all power densities in the absence of stress free boundary conditions in the transparent coating that produces normal forces and subsequently enhances the amplitude of the bulk waves even with low power densities. Among these ultrasound generation mechanisms, the ablation/plasma regime provides a large enhancement of longitudinal (compression) and surface waves amplitude to many folds which is essential for some critical applications, such as online monitoring of thickness of seamless steel tubes and for weld quality monitoring at elevated temperatures [12]. Strong attenuation of ultrasound energy occurs in metals at high temperature which is mainly because of the strong background absorption which increases exponentially with temperature and the scattering by the growth of the grain size from a few 10s of microns to 100s of micron with the temperature increase from 1000° C to 1250° C [6].

A laser source of near IR regions of the laser wavelength is used for metals. The frequency or wavelength of the longitudinal ultrasound depends on the pulse duration of laser which is a limiting factor and it controls the amount of information that can be detected. Usually, thinner samples are measured using high frequency ultrasound and thicker samples with low frequency due to the attenuation of ultrasound in high frequency range. For NDT high resolution measurements in microelectronic structures, the theoretical minimum measurable thickness is one wavelength. So, the thinnest sample or micro void size of μm is measured using short laser pulse (ps) to get high frequency(1GHz) ultrasound signal and hence the shorter wavelengths that are comparable to the sizes. Similarly, moderate duration of the laser pulse (100s of ns) or conventional PZT is used to produce low frequency ultrasound to measure the thicker samples since the attenuation is minimum for low frequency ultrasound [6].

1.3 Detection of ultrasound with a continuous wave laser through optical interferometry

The reflected ultrasound signals from the back surfaces as well as from the defects create a small transient surface displacement (~ 10 nm). These surface displacements can be detected with an interferometer in terms of intensity variations and the detected photocurrents are displayed as voltage output signals with time on an oscilloscope or digitizing electrical processor. As the Fabry -Perot interferometer is less sensitive for low frequencies, there is a need however to measure the surface displacement with rough surfaces, therefore two wave mixing PR interferometers have the best capability to detect broadband signals, were used to overcome these drawbacks. Two wave mixing is a dynamic holographic process where two coherent optical beams (reference beam and signal beam) interfere within a photorefractive crystal (PRC) and the beam emitted from the PR crystals consists of a portion of the

transmitted signal beam and also a part of the reference beam, which is diffracted in the direction of the signal beam. The diffracted reference beam appears to be wave-front matched as it is a holographic replication of the signal beam. These effects can be used to compensate for the distorted wave fronts reflected or scattered from the rough sample surface [13-15]. Furthermore it can also compensate for environmental noise if the grating response time is fast enough to adapt to the low frequency noise by changing the refractive index grating according to the change in the interference pattern with the homodyne interferometer, However, for the mid-frequency noise which arises from the motion of the probed object will change the speckle pattern (phase) of the scattered light or change the frequency by Doppler effect. To compensate for the Doppler shift, heterodyne interferometers can be used where frequency of the one of the beam is shifted to produce vibration free signal at the output [15-16].

1.4 Objective and motivation of the present study

Laser ultrasonics is less sensitive in the detection of tiny surface displacement (pm or few nm), a higher amplitude signal in the ablation regime increases the signal to noise ratio by compensating for the long path length in thick offshore structures. With pulsed laser incidence on the test piece, all three regimes produce longitudinal, shear and Rayleigh (SAW) waves at the same time [10, 12]. Compared to thermoelastic regime, where the amplitude of all the modes increases linearly with the power density, a greater extent of enhancement is observed for longitudinal and SAW waves in the ablation regime than shear waves [10]. The Rayleigh wave penetration depth is dependent on the frequency of the ultrasound, thus if the wavelength is comparable to its thickness, it propagates between the two boundaries of the sample as a Lamb wave [17] or otherwise it remains on the surface as surface skimming waves [18-20]. These surface waves are used to detect the microcracks on the surface and to determine the thickness of thin films with high precision [19-20]. Using longitudinal mode which propagates into the bulk of the material, higher amplitude laser generated ultrasound signal with multiple echoes are observed in the transmission mode to measure the thickness of metals using our system. Furthermore, to measure the remaining thickness of complex structures like corroded oil tubes and pipes, and to detect defects from the internal and surface structures, etc reflection mode signal with pulse echo technique provides a straight forward and less complicated method [21-22]. The simultaneous generation of longitudinal and SAW waves make the detection of ultrasound a challenging one in the ablation regime where the interferometry or the EMAT transducers are sensitive to all modes of the laser generated acoustic waves [12, 23] and hence the reflected longitudinal mode signal from the defect can be masked by other modes, especially by higher amplitude surface skimming waves. In this paper, by utilizing the recent

advances in digital signal processing technique such as the Hilbert transform with other filtering functions, it provides better signal acquisition method and is able to extract detailed features from the defect signal.

2 EXPERIMENTAL PROCEDURES

2.1 Laser ultrasonic system and measurement methods

The experimental arrangement of the integrated laser ultrasonic system which can measure thickness and detect both surface and internal cracks of various metals used in this study is shown in Figure 1. This system consists of a generation laser, optical interferometry detection system and Labview controller for signal analyses. A Nd:YAG laser operating at a wavelength of 1064 nm and a peak energy of 50 mJ/pulse is focused down to 500 microns and then irradiated on the steel surface for ultrasound generation with high spatial resolution. The pulse duration is 8 ns with a repetition rate of 20 Hz. Then the generated ultrasound propagates from the sample front surface to the rear-side surface and the subsequent surface displacement of the transmitted or reflected ultrasound signal is detected by the two-wave-mixing interferometry, where the transmitted signal and diffracted reference are made to interfere in a photodetector to perform phase demodulation using a 532 nm CW laser. Since the surface displacement caused by the ultrasound is very small, high powered CW laser of 213mW is used for detection (see set-up in Figure 1).

With the optimum pulse duration of 8ns, the ultrasound produced has a centre frequency of 23 MHz and the theoretically calculated minimum measurable defect size or thickness value for steel is 0.26 mm (λ) to obtain good sensitivity. Minimum measurable defect sizes depend on the velocity of sound in the material, which also changes significantly with temperature and reduces the measurement accuracy. In general, the thickness and the defect of the material can be measured using one of the ultrasonic non-destructive testing technique, such as pulse echo [8], resonance [24], or Lamb wave [17]. Though the pulse echo method is a simple technique to implement for real life applications, thinner samples (less than 1mm) are difficult to be measured accurately. It is because the time interval between the incident and echo pulse is very short and overlapping may occur between two successive pulses for metals whose acoustic velocities are high. For precise and high time resolution measurements of thinner samples, the short time interval between the two successive pulses can be recorded using higher frequency ultrasound pulse that has short pulse width and fast response detector with bandwidth of 1GHz. Using our available laser ultrasonics system with our high response time APD detector, we could measure 0.5 mm thick aluminum sample. Despite the center frequency of 23 MHz, the signal contains broad optical side bands as well. The unipolar stress signals in ablation regime have strong

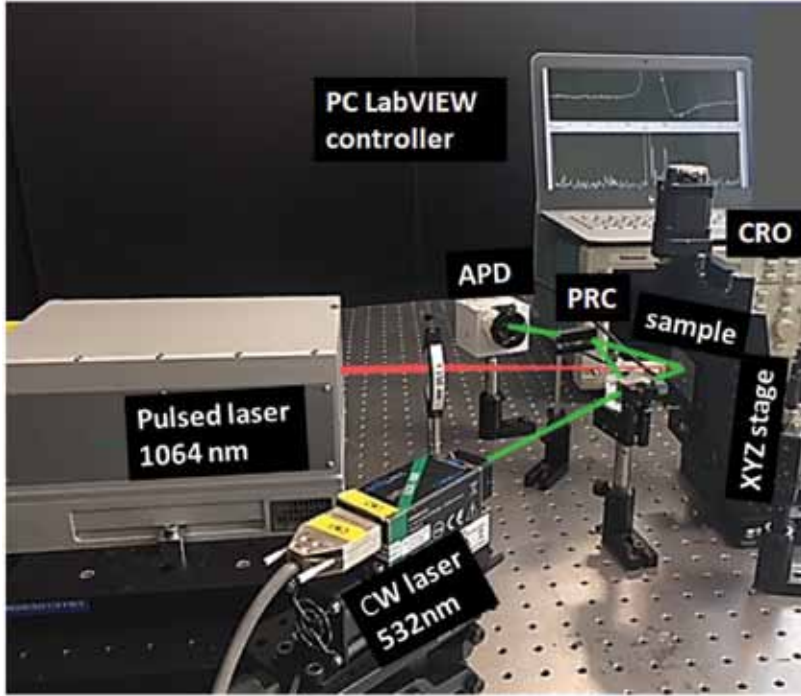


FIGURE 1
Integrated laser ultrasonic system in reflection mode.

low frequency components thus allowing low frequency ultrasound waves to propagate at longer distances such as thicker (60 mm) samples without much attenuation. Thus, this laser based ultrasonic detection system has a unique advantage with higher sensitivity on rough surfaces, better spatial resolution and more tolerance to the industrial vibrations and object motions.

3 RESULTS AND DISCUSSION

3.1 Problems associated with signal detection in the reflection method

Figure 2a shows the acquired ultrasound signal for thickness measurement in transmission mode. The waveform shows higher amplitude signal with multiple echoes. In the reflection mode, the same laser ultrasonic system is used with similar experimental conditions as in transmission mode except both beams are irradiated on the same side of the sample for generation and defect detection. There are some issues related with the interaction between the generation and detection spots that are in the adjacent regions. Mainly, the sensi-

tivity of the surface displacement of the detection spot is distorted by the generation mechanism when two beams are kept close to each other and hence a very weak signal is observed in the reflection mode. Furthermore, the strong surface waves which propagate along the interface is interfering with the reflected longitudinal mode signal. In contrast, the surface skimming waves propagates only on the generation side in the transmission mode, hence the detection of the longitudinal mode signal is not affected by these surface waves. Therefore, some gap between the generation and detection beam is maintained to increase the sensitivity (surface roughness) of the surface displacement from the unaffected spot and also to avoid the interference by surface waves if the arrival time of the longitudinal is shorter than the surface waves.

If the detection and generation beams are kept apart with some distance over 2mm, the normal incident waves are reflected back without much deviation from the normal direction, that creates the problem of detection loss whereby the detection laser spot is away from the irradiation spot and this can be explained by the directivity of ultrasound propagation [25-26]. As the ultrasound waves generated by ablation regime are very sensitive to the incident angle, the wave propagation is mostly in the force direction. Since we used generation beam with normal incidence in order to measure actual values by the shortest propagation path, the longitudinal wave propagates in the force direction and thus multiple reflections from the rear side can reach normal to the surface. In Figure 2b, two beams are kept 2mm apart, so the first echo (T1) which is normal to the surface doesn't reach the detection spot and only slightly deviated higher order echoes would reach the detector. Therefore, an optimized distance of ~1mm is kept between the two beams without ablating the detection spot in order to increase the sensitivity, at the same time to acquire the first echo. The signal in Figure 2c shows multiple echoes including the first echo (T1) are observed which often overlaps with the tail of the strong surface waves for a sample that is 4mm thick. For the reflected signal from the defect or the rear side of thinner samples (~ 1mm), the signal will mostly be overlapped or hidden in the tail of the surface waves causing the determination of the arrival time of the ultrasound to be complicated. It is reported that to separate the longitudinal modes from the surface waves and other mode converted waves which have different acoustic velocities, a large gap is given between the two beams to maximise the difference in their arrival times. Ultimately, the signal reaches the receiver end after multiple reflections, but the signal, especially reflected from the defect has lower amplitude and minimal information can be deduced. Studies have also shown that frequency spectra analysis with hanning window is used to extract the useful longitudinal mode signals in time of flight measurements where all the modes are mixed in ablation regime. Some authors have designed directional EMAT to acquire the required laser generated ultrasound mode. Extra or the missing feature in the A scan will indicate the scattered signal from the defect in the

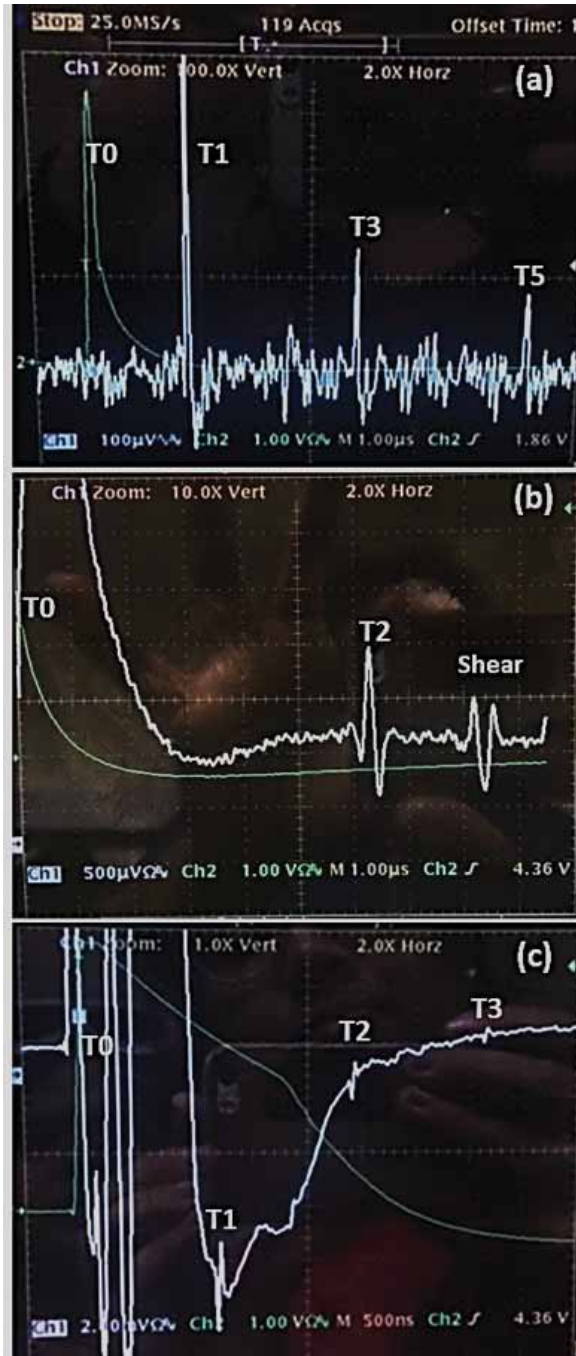


FIGURE 2 Laser ultrasonic signal from Al sample a) in transmission mode b) and c) in reflection mode, with varying the distance between two beams at 2mm and 1mm, respectively.

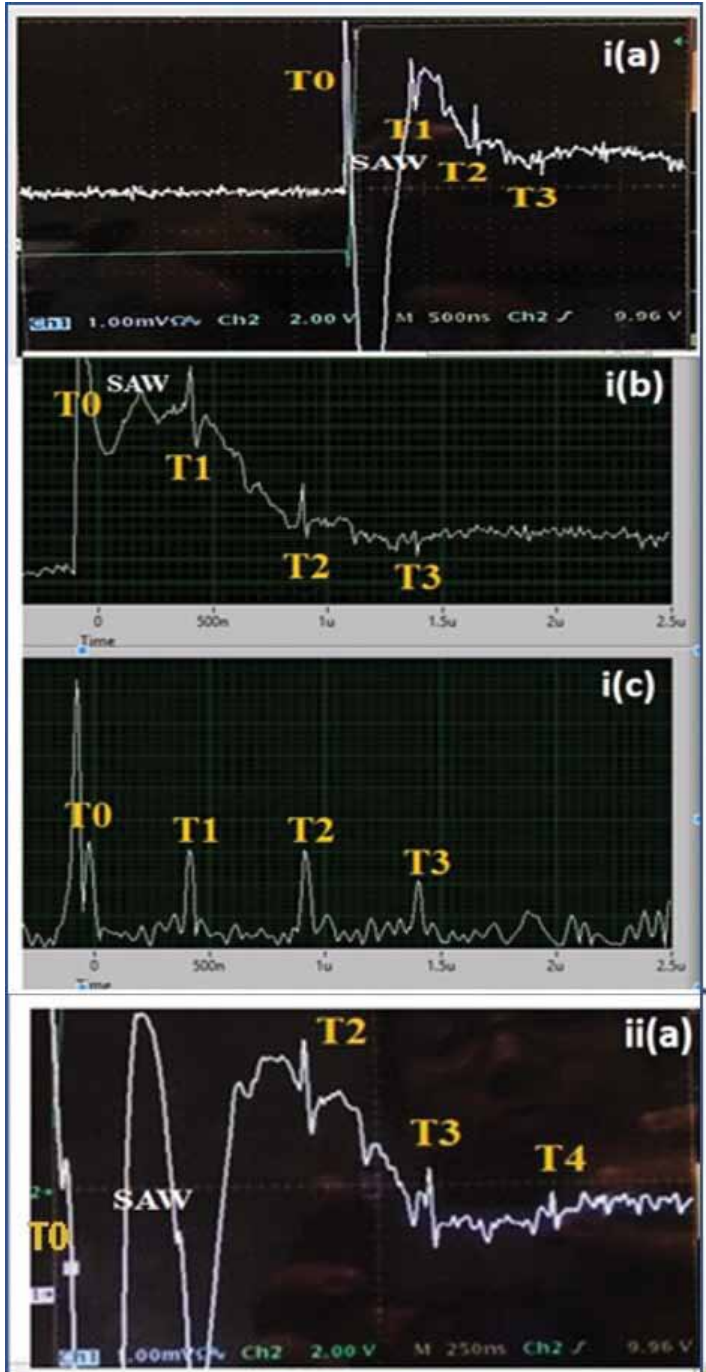
longitudinal signal. It may also be possible to detect surface breaking crack if the surface waves are disrupted. In all these cases, there was a disagreement between the line scan A and scan image B [12, 23].

3.2 Solutions to extract useful longitudinal mode signal

Utilising the property of varying frequency components of the bulk and surface waves, the desired frequency components of the longitudinal signal from the surface waves can be filtered. In most cases, the surface waves have a lower frequency distribution compared with the frequency spectra of bulk waves [12]. In practice, frequency domain analysis has been done with the original signal to determine frequency distribution and is then used with a properly designed selective filter to obtain the required signal from the low frequency surface waves. Subsequently, the inverse Fourier transform is applied to get the desired signal in the time domain to determine the arrival time of the reflected signal from the rear side and the defects for defect locations. Although frequency domain analysis would be more appropriate for some functions, such as filtering (convolutions), design systems, reconstruction of signals and reduction of noise, in a case where the signals are more likely complex and mixed, the selective band pass filter provides a longitudinal mode signal from the SAW. However, there is a possibility of the presence of some mid frequency component from the surface wave in the filtered signal. Furthermore, FFT would not give accurate information in both frequency and time domains simultaneously for waveforms like ultrasound signals that are nonlinear and non-stationary in nature. Moreover, to scan the entire sample, there is a need to set positive threshold voltage values in B and C scan, as the signal detected might have a stronger negative peak than positive in tripolar waveforms. Hilbert transform phase shifts all the positive frequency signals by $-\pi/2$ and negative frequencies to $\pi/2$ and hence it gives out an instantaneous amplitude and frequency of the component that describes the signal more locally in the time domain [27-29]. Therefore, with a selective band pass filter followed by the Hilbert transform, the phase shifting of the signal into fully positive signals by Hilbert transform helps to locate and identify the signal with an increase in instantaneous amplitude and pulse width. This is due to the combined effect of the phase shifted mono frequency components from the presence of other high frequency component of the surface wave.

3.3 Single unipolar waveforms obtained with filter followed by Hilbert transform

Comparative studies using various sequences of filtering functions with HT are carried out. Figure 3a shows the oscilloscope image of the reflected signal from a 1.5mm steel sample. Although the signal has a higher amplitude, it is overlapped with a surface wave. The subsequent waveforms in Figure 3b and Figure 3c are obtained after processing the original waveform (Figure 3a) in the oscilloscope with the Hilbert transform and filter functions in LabVIEW.



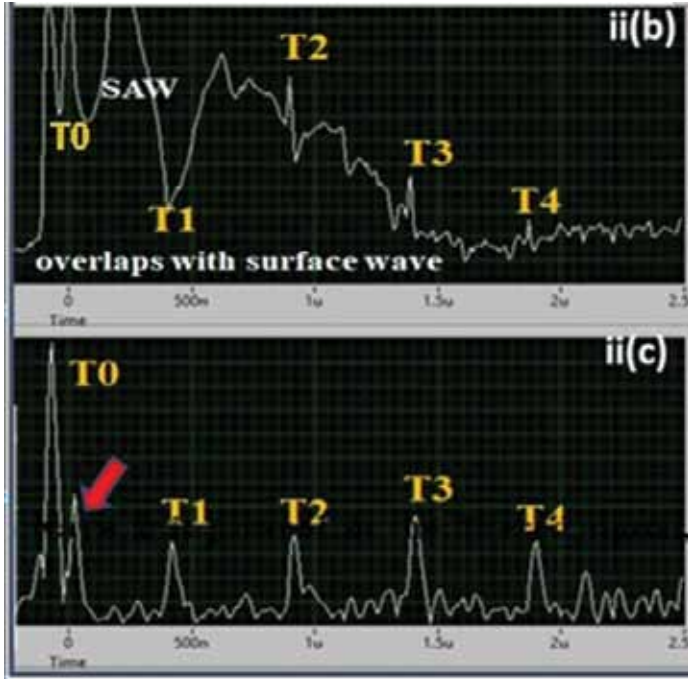


FIGURE 3

Overlapping of ultrasound signal with (i) weak and (ii) strong surface waves amplitude (a) waveform obtained directly from the oscilloscope to the labview (b) signal processing using HT only, (c) bandpass filter followed by HT.

The signal processing of the original signal using only Hilbert transform (HT) shows a clear and distinct first echo (Figure 3i(b)). Figure 3i(c) shows the signal obtained with band pass filter followed by HT. However, the signal is hidden completely in the original waveform as shown in Figures 3ii (a&b) for samples that exhibit weak reflected signal or with strong surface waves. The filtering functions followed by HT provides a distinct signal with few echoes and there is also a presence of some mid frequency component in the waveform near T0 (indicated with a red arrow in Figure 3ii(c)). This may lead to the inaccurate location of an unknown test specimen. The phase shifted positive signal from Hilbert transform increases the instantaneous amplitude and pulse width and thus helps to locate and identify the signal more easily, shown in Figure 4b. For example, a high frequency component in the waveform for the first order is at 500ns, second at 1000ns, etc. (indicated in arrow) is compared with Figure 4a in which the waveform is obtained directly from the oscilloscope to the LabVIEW without Hilbert transform. Frequency analyses using FFT are done to know the frequency distribution of the signal and

SAW waves generated using laser pulse having 8ns pulse duration, so that proper filtering bandwidth can be chosen to separate the signal. The frequency spectrum of the original signal from the oscilloscope is shown in Figure 4c. The frequency distribution of the surface wave mainly resides from 1 to 25MHz, and the longitudinal signal is between 25 to 50MHz.

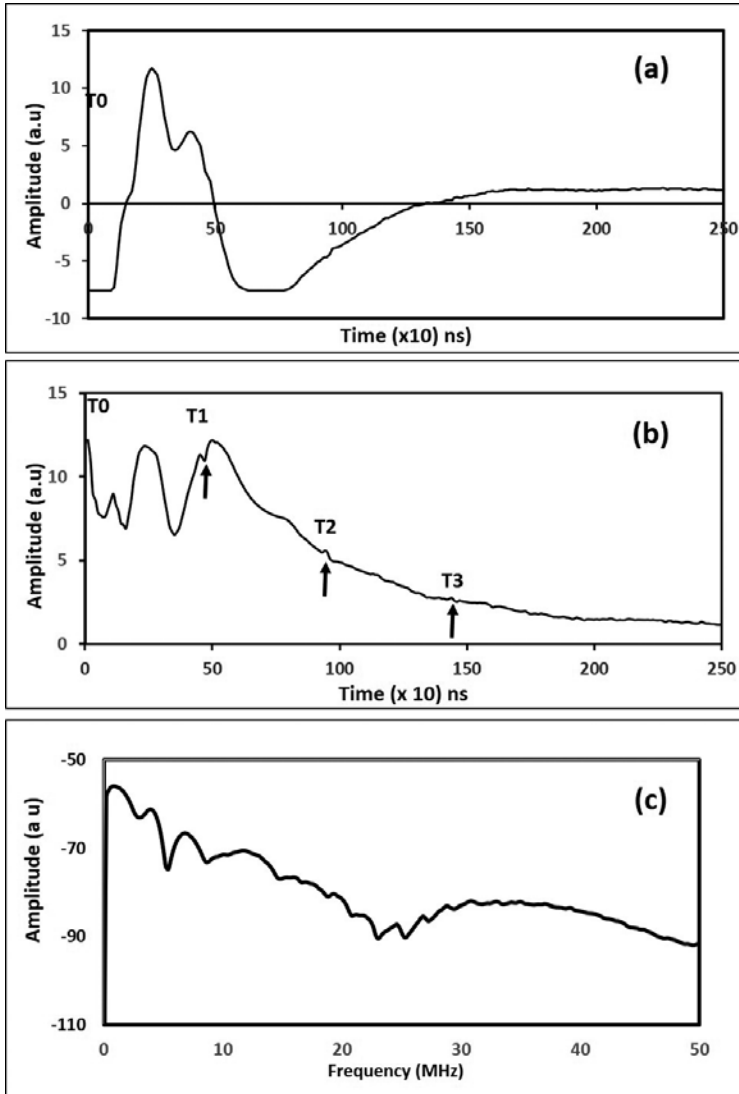


FIGURE 4

(a) Waveform obtained directly from the oscilloscope to the labview, (b) signal processing of the original signal using HT and (c) the FFT spectrum.

Systematic studies have been done with the same original signal from Figure 4a with three different sequences of filtering functions and HT. Figure 4a shows a strong amplitude from surface waves and the longitudinal signal is overlapped or hidden completely. A band pass, butterworth filter with the 3rd order is selected and lower cut off frequency is set at 25MHz and highest cut off frequency at 50MHz. In the first approach, only a filter was used to separate the signal (Figure 5a) and in the second, the Hilbert transform is applied first followed by a filter (Figure 5b), and hence both approaches separates the weak useful signal from surface waves and provides distinct ultrasound sig-

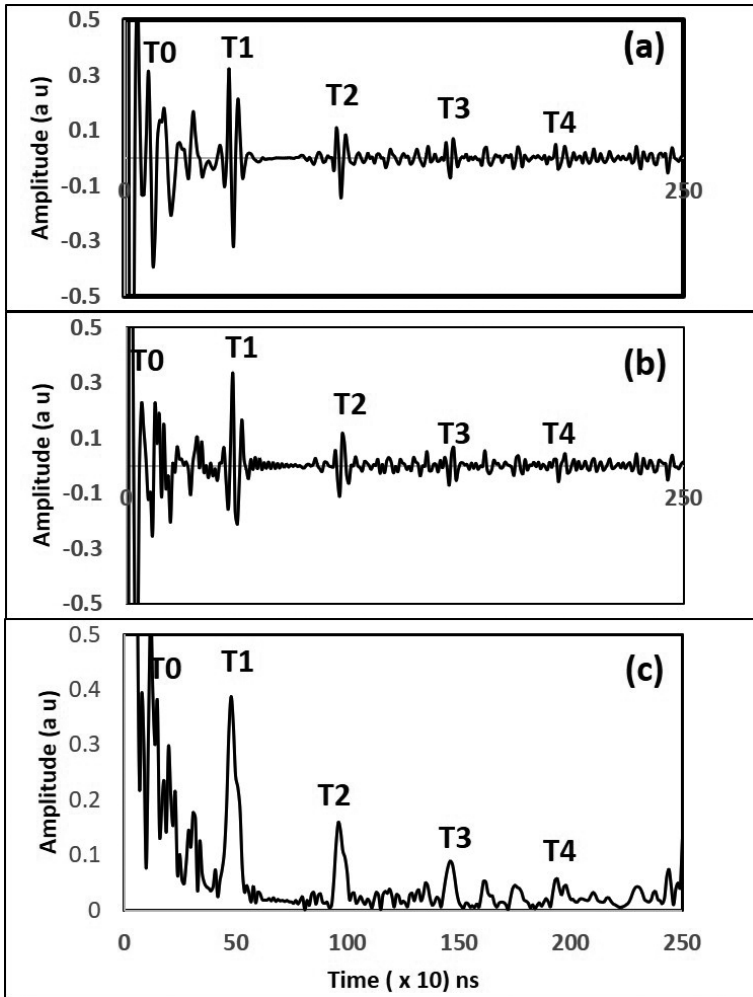


FIGURE 5

Comparative studies of the original signal with varying sequence of filtering functions with HT. A) filter only, b) HT followed by filter and c) filter followed by HT.

nal with tripolar waveform (two positive peaks with a trough) although with high frequency noise in HT-filter combination. In the third approach, we used a filter first followed by the Hilbert transform. Hence this phase shifts all the filtered signals into a positive peak, giving one clear distinct peak with an increase in the amplitude from the rest of the high frequency noise that improves the signal to noise ratio by denoising (5c). Single, distinct, unipolar waveform is obtained with these bandpass filters followed by HT combination than with the tripolar signal. It is usual that the ultrasound signal may have only negative or weak positive peak voltage, so the phase shifted positive signal by HT is essential for B and C scans where the threshold voltages are set by the positive peak values.

3.4 Acquiring signal from defect using this signal processing approach

In Figure 6i(b), despite the clear first echo in 10mm thick sample, there is an absence in the defect signal which is expected to be between T0 and T1 caused by a tendency of overlapping with SAW waves. However, with a filter followed by HT, a clear distinct defect signal is observed from the tail of the SAW, as indicated in Figure 6ii(b). The T1 amplitude is lesser, since part of the ultrasound signal is reflected from the defect. The amplitude of the signal can be increased with a low noise amplifier. Usually for denoising, filtering and compression, various signal processing techniques in time and frequency domain signals such as SIFT, wavelet transform, etc. are used. From the detailed study of the frequency spectral analysis in the ablation regime, the distribution of the spectrum is mainly dependent on the material, thickness, and laser power density and hence the frequency spectra is used to identify the defect signal [12]. Hilbert Huang transform decomposes the signal into different intrinsic modes functions in the sifting process, by separating the desired signal is applied for the ultrasonic inspection of oil pipes and highly attenuating structures using PZT [27-28]. From the frequency component of the marginal spectrum which is calibrated from the IMF modes of time domain signal, the HHT is used to determine the defect characteristics [30]. The signal processing method proposed in our studies using a filter followed by Hilbert transform phase shifts the mono frequency components in the low frequency oscillatory signal thus showing a more distinct identification of defect features from the complex signal with the presence of multimode, environmental (excitation laser intensity) and electrical noises and multiple reflections from the interfaces.

4. CONCLUSION

We have successfully extracted the useful longitudinal mode ultrasound signal from the surface waves with filter followed by the Hilbert transform. The Hilbert transformed signal shows the instantaneous amplitude for high fre-

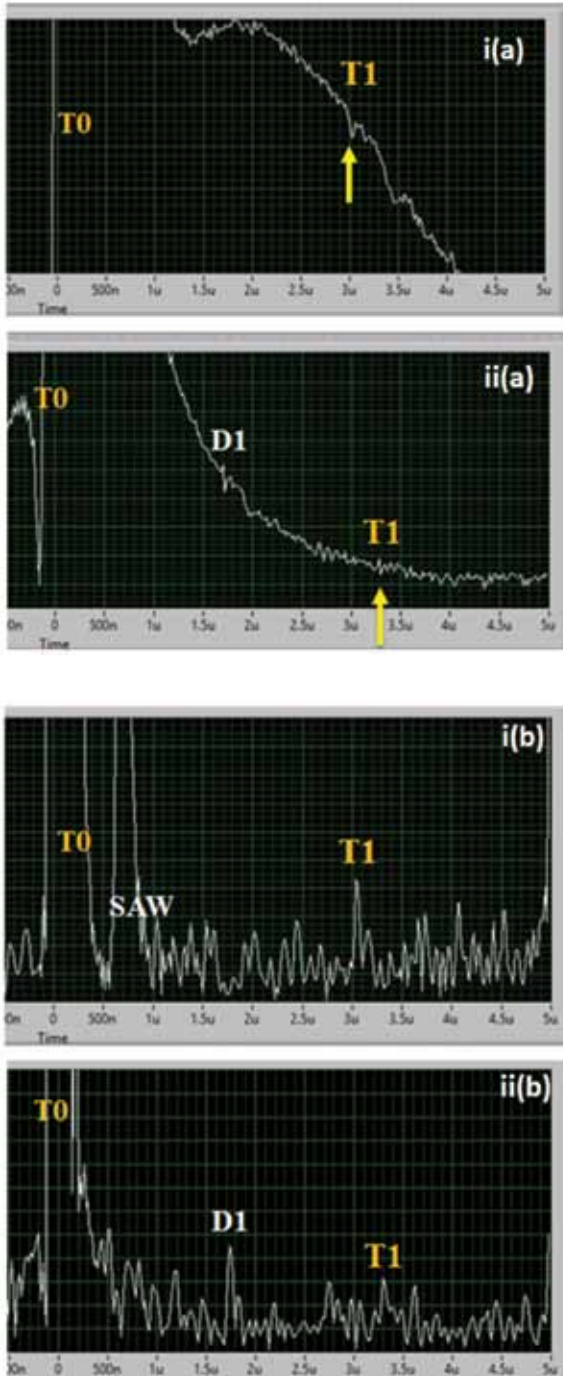


FIGURE 6
Weak defect signal observed from the tail of the surface wave with a) HT only and b) HT and filter.

quency longitudinal signal which is used as a reference to identify the desired signal with the filter. The combination of filter followed by HT gives a single positive peak with higher amplitude and improved SNR which is essential to set the positive threshold voltages for B and C scan. Integrating this signal processing method with a portable laser ultrasonic scanning system, high signal to noise ratio can be achieved without the use of a high voltage supply for the photorefractive crystal in the two-wave mixing interferometer.

ACKNOWLEDGEMENT

This research was supported by the Singapore Maritime Institute (SMI) research project (SMI-2015-OF-10).

REFERENCES

- [1] Mitra M. and Gopalakrishnan S. Guided wave based structural health monitoring. *Smart Materials and Structures* **25** (2016), 053001-053027.
- [2] Birks A. S., Green, Jr. R. E. and McIntire, P. *Nondestructive Testing Handbook, Ultrasonic Testing*, 2nd Edition. American Society for Nondestructive Testing, (1991).
- [3] Monchalín J. P. and Wagner J. *Nondestructive Testing Handbook, Ultrasonic Testing*, 2nd edition. American Society for Nondestructive Testing, Columbus, (1991).
- [4] Kozhushko V. V. and Hess P. Nondestructive evaluation of microcracks by laser-induced focused ultrasound. *Applied Physics Letters* **91** (2007), 224107.
- [5] Monchalín J. P., Choquet M., Padioleau C., Néron C., Lévesque D., Blouin A., Corbeil C., Talbot R., Bendada A., Lamontagne M., Kolarik R. V., Jeskey G.V., Dominik E. D., Duly L. J., Samblanet K. J., Agger S. E., Roush K. J. and Mester M. L. Laser ultrasonic system for on-line steel tube gauging. *Review of Quantitative Nondestructive Evaluation, AIP Conference Proceedings* **657** (2003), 264.
- [6] Kruger S. E., Lord M. and Monchalín J. P. Laser ultrasonic thickness measurements of very thick walls at high temperatures. *AIP Conference Proceedings* **820** (2006), 240-247.
- [7] Scruby C.B. and Drain L.E. *Laser Ultrasonics: Techniques and applications*, UK Bristol: Adam Hilger, (1990).
- [8] Monchalín J. P. Progress towards the application of laser -ultrasonics, Review of Progress in Quantitative Nondestructive Evaluation, Vol. 12 Edited by D.O. Thompson and D.E. Chimenti, Plenum Press, New York **12** (1993), 495-506.
- [9] Dubois M. and Drake Jr. T.E. Evolution of industrial laser-ultrasonic systems for the inspection of composites. *Nondestructive Testing and Evaluation* **26** (2011), 213-228.
- [10] Daviest S. J., Edward C., Taylor G. S. and Palmer S. B. Laser-generated ultrasound: its properties, mechanisms and multifarious applications. *Journal of Physics: D Applied Physics* **26** (1993), 329-348.
- [11] Murray T. W. and Wagner J. W. Thermoelastic and ablative generation of ultrasound: Sound effects, *Review of Progress in Quantitative Nondestructive Evaluation*, Vol 17 Edited by D.O. Thompson and D.E. Chimenti, Plenum Press, New York. 1998. 17, 619-625.
- [12] Mi1 B. and Ume1 I. C. Parametric studies of laser generated ultrasonic signals in ablative regime: time and frequency domains. *Journal of Nondestructive Evaluation* **21** (2002), 23-33.
- [13] Blouin, A. Drolet. D. and Monchalín J.P. Ultrasonic detection system based on two wave mixing in photorefractive effect. *Review of Pogress in Quantitative Nondestructive Evaluation* **14** (1995), 2245-2251.

- [14] Ing R. K. and Monchalín J.-P. Broadband optical detection of ultrasound by two-wave mixing in a photorefractive crystal. *Applied Physics Letters* **59** (1991), 3233-3235.
- [15] Pouet B.F., Ing R.K., Krishnaswamy S. and Royer D. Adaptive heterodyne interferometer for ultrasonic NDE. *Review of Progress in Quantitative Nondestructive Evaluation*, Edited by D.O. Thompson and D.E. Chimenti., Plenum Press, New York, **17**, 1998.
- [16] Pouet B. F., Ing R.K., Krishnaswamy S. and Royer D. Heterodyne interferometer with two-wave mixing in photorefractive crystals for ultrasound detection on rough surfaces. *Applied Physics Letters* **69** (1996), 3782-3784.
- [17] Prada C., Balogun O. and Murraya T. W. Laser-based ultrasonic generation and detection of zero-group velocity Lamb waves in thin plates. *Applied Physics Letters* **87** (2005), 194109-(3).
- [18] Hess P. Surface acoustic waves in materials science. *Physics Today* **55** (2002), 42-47.
- [19] Dewhurst R. J., Edwards C. and Palmer S.B. Noncontact detection of surface-breaking cracks using a laser acoustic source and an electromagnetic acoustic receiver. *Applied Physics Letters* **49** (1986), 374-376.
- [20] Clorennec D. and Royer D. Analysis of surface acoustic wave propagation on a cylinder using laser ultrasonics. *Applied Physics Letters* **82** (2003), 4608-4610.
- [21] Zamiri S., Reitingner B., Bauer S. and Burgholzer P. Converging Laser Generated Ultrasonic Waves using Annular Patterns Irradiation. *3rd International Symposium on Laser Ultrasonics and Advanced Sensing IOP Publishing Journal of Physics: Conference Series* **520** (2014), 012001.
- [22] Jacobs L. J. and Whitcomb R. W. Laser generation and detection of ultrasound in concrete. *Journal of Nondestructive Evaluation* **16** (1997), 57-65.
- [23] Dixon S., Edwards C. and Palmer S.B. A laser-EMAT system for ultrasonic weld inspection. *Ultrasonics* **37** (1999), 273-281.
- [24] Sen C. and Tie G. Ultrasonic thickness measurement for aluminum alloy irregular surface parts based on spectral analysis. *Trans. Nonferrous Met. Soc. China* **22** (2012), s323(1-6).
- [25] Guo Y., Yang D., Chang Y. and Gao, W. Effect of oblique force source induced by laser ablation on ultrasonic generation. *Optics Express*, **22** (2014), 166 -176.
- [26] Raetz S., Dehoux, T. and Audoin, B. Effect of laser beam incidence angle on the thermoelastic generation in semi-transparent Materials. *The Journal of the Acoustical Society of America* **130** (2011), 3691.
- [27] Kazys R., Tumsys O. and Pagodinas D. Ultrasonic detection of defects in strongly attenuating structures using the Hilbert- Huang transform. *NDT&E International* **41** (2008), 457- 466.
- [28] Sudheera K., and Nandhitha N. M. Application of Hilbert transform for flaw characterization in ultrasonic signals. *Indian Journal of Science and Technology* **8** (2015), 56303-56309.
- [29] Grünsteidl I., Veres I. A., Roither J., Burgholzer P., Murray T. W. and Berer T. Spatial and temporal frequency domain laser-ultrasound applied in the direct measurement of dispersion relations of surface acoustic waves. *Applied Physics Letters* **102** (2013), 0111039(1-4).
- [30] Mao Y., Que P. and Zhang Q. Ultrasonic thickness inspection of oil pipeline based on marginal spectrum of Hilbert-Huang transform. *17th World Conference on Nondestructive Testing*, 25-28 Oct 2008, Shanghai, China, PP 1-8.

Investigation on High Power Laser Removal of Thermal Barrier Coating (TBC) and Bond Layer (MCrAlY) from Inconel 718 Alloy

J. C. HERNANDEZ-CASTANEDA, W. Y. CHI, F. YONGWEI, NG F. LAN,
M. C. C. KHIN AND Z. HONGYU*

¹*Singapore Institute of Manufacturing Technology, 2 Fusionopolis Way, #08-04, Innovis, 138634, Singapore*

²*School of Mechanical Engineering, Shandong University of Technology, Zibo, Shandong, China*

This paper reports the development of a precise laser removal process of thermal barrier coating (TBC) and bond layer (BL) from aero engine components as an alternative method to hazardous chemical bath processes. A high power Nd:YAG laser ($\lambda=1064$ nm, $\tau=38$ ns) system was successfully employed to remove yttria-stabilised zirconia (TBC) coating and bond layer (MCrAlY) from equiaxial grain Inconel 718 alloy. Investigation on the different assisting media and process conditions to remove TBC coating by high power pulsed laser are reported. A parametric investigation of direct laser removal process of the TBC coating established optimal conditions to achieve 140 mm³/min removal rate. A novel two-step laser scanning method was developed to remove the bond layer coating at 10 mm³/min and with a minimal recast layer of 4 μ m thickness. A wavelength-dispersive X-ray spectroscopy (WDS) analysis identified the chemical composition of the laser cleaned surfaces for the complete set of conditions tested. It was found that low oxidation levels were attained when the laser beam was scanned at 14 kHz followed by a 6 kHz laser beam scan which is also the optimal condition for the highest material removal rate. An X-ray diffraction (XRD) analysis identified the type and magnitude of residual stresses after the laser cleaning process. The measured residual stresses are tensile in nature with an average magnitude of 547 MPa, which are comparable to those observed in laser additive processes.

Keywords: laser removal, thermal barrier coating, bond layer, MCrAlY, Inconel 718

Corresponding author's e-mail: hyzheng@simtech.a-star.edu.sg

1. INTRODUCTION

Laser surface treating of super alloys has attracted attention of the scientific community in recent years [1-17]. However, research on laser cleaning had focussed on areas such as Nd:YAG and CO₂ lasers preparation of titanium alloy components for joining by electron beam (EB) welding and diffusion bonding by Turner *et al.* [5-8]. Oltra and co-workers reported an enhanced oxide film removal from metal surfaces (steel substrate) by the application of pulsed laser irradiation in a liquid confinement at controlled electrochemical potential [9]. Sezer, H.K. *et al.* [10-12] have reported bond layer (BL) and thermal barrier coating (TBC) delamination mechanisms and the effects of a coaxial and a secondary gas jet (with different angles) on the material ejection process while drilling acute angled holes, typically found on aero-engine components, on Nickel alloys with BL/TBC coatings. Feng Q. *et al.* [13] employed a Ti:sapphire femtosecond laser to drill single-crystal superalloy Rene N5 through thermal barrier coatings and bond coat (MCrAlY) without defects such as delamination, recast layer or spatter. More recently, different types of lasers have been employed in selective laser sintering of Inconel 718 for three dimensional printing and repair of valuable components [14-17]. Jia and Gu investigated the effect of laser energy input in selective laser sintering of Inconel 718 which modified the microstructure, hardness and wear resistance properties of the produced elements [14]. Bennett, J. *et al.* found that longer cooling and solidification rates of laser deposited Inconel 718 generated coarser microstructures which reduced the ultimate tensile strength of the deposited elements [16]. The generated phases in pulsed Nd:YAG laser deposition of Inconel 718 and their effect on stress rupture behaviour of elements was reported by Sui S. *et al.* [17].

Modern hot section aero engine components are commonly coated with corrosion resistant and thermal barrier coatings. During an overhaul cycle, these coatings need to be removed before any repair can be performed. The coating thickness may vary due to conditions such as coating location (e.g. leading or trailing edge of a vane), tolerance in the coating thickness during the application process, diffusion of the coating during engine run and coating chip-off that may occur due to handling and engine operation.

Various methods have been proposed for the removal of TBC for turbine components including the use of shockwaves [18, 19], abrasive water jets [20-22] as well as initial explorations with lasers [23]. The current method to strip TBC and BL coatings from the aero engine components includes the combined use of abrasive blasting and acid baths. However, due to coating variation, components' shape contour, and the cooling holes configuration, employing these two methods may cause excessive wear on the parent material on some areas and leave remnant coating on other locations. Furthermore, acid stripping can also result in stress corrosion cracking and alloy depletion. Therefore, a stripping/cleaning system that is fast and able to

remove coating without affecting the base metal will be of interest for aerospace maintenance repair and overhaul industry. To this end, this research work explores for the first time, in a systematic and comprehensive experimental approach, the capability of a laser cleaning process as an alternative method for the removal of TBC coating and BL. Lasers are precise, powerful and contactless tools capable of removing almost all kinds of materials given the selection of the right wavelength, power level and temporal interaction (pulse duration). These advantages have allowed their exploration of multiple lasers on the removal of coatings, paints and contaminants from various types of metals and concrete substrates [24-26] relevant to multiple industrial applications. Moreover, computer programmable beam delivery through optical fibres combined with galvanometer-scanners and programmable focussing optics allows flexible and precise laser beam delivery over three dimensional shapes [27]. Here, the explored laser removal method aims to build a foundation for an effective and automated approach for the removal of TBC and BL coatings from aero-engine components, without introducing additional waste to the cleaning system. In this contribution, a high power Nd:YAG laser ($\lambda=1064$ nm, $\tau=38$ ns) system is investigated to remove the TBC and BL coatings from equiaxial Inconel 718 alloy typically employed in the manufacture of aero engine components. Since laser cleaning is a thermal process, the quality criteria were based on the degree of side-effects such as surface oxidation, melting and crack development, micro-structural changes, and residual stress on the metal substrates as well as the achievable material removal rates. The effects of the high-intensity laser interaction with the Inconel 718 alloy were analysed and the findings discussed.

Different assisting media were explored to improve the material removal rate of thermal barrier coating (TBC) and the quality of the laser cleaned surfaces as well as to optimise the consumption of energy. A novel two step laser scanning method was developed for the removal of the tough interfacial bond layer (BL) at competitive rates, with low oxidation level and minimal recast layer. The chemical and mechanical integrity of the laser cleaned surfaces under different process conditions were investigated through WDS and XRD analyses as well as optical and SEM microscopy inspection.

2. MATERIALS AND METHODS

A nickel base alloy equiaxial Inconel 718 coupons with chemical composition shown in Table 1 were employed in this work. This Nickel base alloy has a polycrystalline structure with fine grains given its solution annealing condition (AMS 5596). The coupons have the following dimensions 50 x 45 x 3 mm; they were thoroughly cleaned by acetone wiping and ultrasonic bath (30 minutes) to remove any contaminants from their surfaces. The coupons were first coated with 350 μ m bond layer (BL) MCrAlY with a chemical composi-

TABLE 1

The chemical composition of Inconel 718 employed (in weight percent, wt%).

C	Mn	P	Si	Cr	Ni	Al	Mo	Cu	Cb	Ta	Ti	Co	B	Fe
0.05	0.08	0.005	0.05	18.26	51.72	0.62	2.89	0.04	5.04	0.01	1.01	0.38	0.003	19.83

TABLE 2

The chemical composition of bond layer coating (MCrAlY) (in weight percent, wt%).

Ni	Cr	Al	Y	Co
32	21	8	0.5	Balance

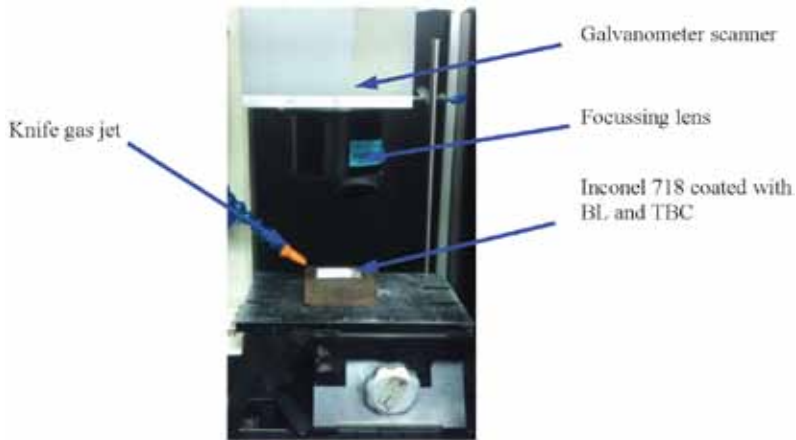


FIGURE 1

Experimental set up for the laser removal of TBC and BL (MCrAlY).

tion shown in table 2 and then coated with 1 mm Ytria-stabilised zirconia (8%). The coating method was low-pressure plasma spray (LPPS) for the bond layer, followed by a diffusion stage and finally atmosphere plasma spray (APS) for top coat (TBC).

A high-power laser beam was directed at the TBC and bond layer to cause thermal ablation and their removal. A pulsed mode Nd:YAG laser (DQ x50 S, ROFIN Baasel, GbmH) $\lambda=1064$ nm, $\tau=38$ ns with an adjustable repetition rate of 6 – 15 kHz and maximum average power of 500 W was employed for the cleaning operation. The laser beam was delivered by a 600 μm squared core optical fibre to a collimating unit and into a galvanometer scanner. A telecentric f-theta lens ($f=80\text{mm}$) focused the laser beam into a top hat square spot of 0.6 mm. Figure 1 shows the experimental set up for the multiple experiments conducted in this research work.

Multiple laser removal techniques and the application of different assisting media were explored. A parametric investigation for the removal of TBC and BL from flat samples was conducted under different pulse duration, repetition rates, laser power level, scanning patterns and speed. Furthermore, process optimisation was followed to maximise material removal rates, minimise thermal effects, and improve surface quality.

2.1. Material Characterisation

The laser removal of thermal barrier coating (TBC) was analysed by optical microscopy. The samples ablated by the laser beam were measured with an Optical Microscope (MX51, Olympus, Corp.) coupled with an image analyser software.

Metallurgical analyses were conducted to determine thermal effects, material degradation and surface quality of laser cleaned samples. The Inconel 718 coupons with the bond layer (MCrAlY) stripped by the laser ablation process were cross-sectioned and mounted on hard ceramic for grinding and polishing. An etchant solution was prepared with the composition of 15 ml hydrochloric acid (HCl), 10 ml acetic acid (CH_3COOH) and 10 ml of nitric acid (HNO_3) to analyse the grain structure on the surface irradiated by the laser beam through optical and SEM microscopy. A scanning electron microscope (SEM) (EVO50, Carl Zeiss, AG) was employed to inspect the presence of re-solidified material (recast layer thickness) through chemical etching. This system was coupled with an EDX analyser to verify the elemental composition of the recast layer. A field emission scanning electron microscope (FE-SEM) (Ultra Plus, Carl Zeiss, AG) was employed for a wavelength-dispersive X-ray spectroscopy (WDS) analysis to verify if the bond layer coating was completely removed and to measure the oxidation level present on the laser cleaned surfaces. Finally, an X-ray diffractometer ($\mu\text{-X360s}$, Pulsetec USA, Inc.) was employed for X-ray powder diffraction (XRD) analysis to determine residual stress on the laser cleaned substrates.

2.2. Laser removal of thermal barrier coating (TBC)

Laser ablation of the TBC (Yttria-stabilised zirconia 8%) was first investigated. A series of preliminary tests identified feasible conditions to remove this material. Small areas were employed to tests various process conditions. The TBC coated coupons were sectioned into smaller test pieces. Tracks of 2 mm width by 12.5 mm length were cleaned through multiple passes of the laser beam directed by the galvanometer scanner. The laser beam movement paths were tested at 70 and 80 % overlapping. Five power levels 400, 412.5, 425, 437.5 & 450 W and two locations of the beam focal point position (i.e. at top and bottom of the TBC coating) were tested. The laser beam was scanned at 975 mm/s and 50 passes were applied in each test in a dry condition. The use of two different media i.e. Argon gas jet and low-pressure water steam was explored to analyse their effect in the laser removal process. Table 3 lists all the tests conducted.

TABLE 3

Laser process conditions tested in the removal of thermal barrier coating - TBC - (Yttria-stabilised zirconia 8%).

Test No.	Condition	Beam overlap (%)	Focal point position (mm)	Power level (W)
1	Dry	70	0	400
2	Dry	70	0	412
3	Dry	70	0	425
4	Dry	70	0	437
5	Dry	70	0	450
6	Dry	70	-1	400
7	Dry	70	-1	412
8	Dry	70	-1	425
9	Dry	70	-1	437
10	Dry	70	-1	450
11	Dry	80	0	400
12	Dry	80	0	412
13	Dry	80	0	425
14	Dry	80	0	437
15	Dry	80	0	450
16	Dry	80	-1	400
17	Dry	80	-1	412
18	Dry	80	-1	425
19	Dry	80	-1	437
20	Dry	80	-1	450
21 - 30	Argon gas	75	0, -1	400, 412, 425, 437 450
31 - 40	Water steam	75	0, -1	400, 412, 425, 437 450

The trials with assisting media followed similar conditions differing only on the laser beam overlap at 75%. A diagram of the sample sectioning and the various conditions tested to assist the removal of the TBC coating are shown in figure 2. The conditions investigated included dry ablation of TBC, the use of an assisting Argon gas jet and the application of a low-pressure water steam jet. The complete removal of the coating, under various conditions, was verified through optical microscopy. The area of removed TBC coating was measured at the cross section of all laser ablated samples and the total volume of removed material was computed. The expenditure of energy was then calculated from the process parameters. An energy consumption was computed from all conditions tested by the following equation:

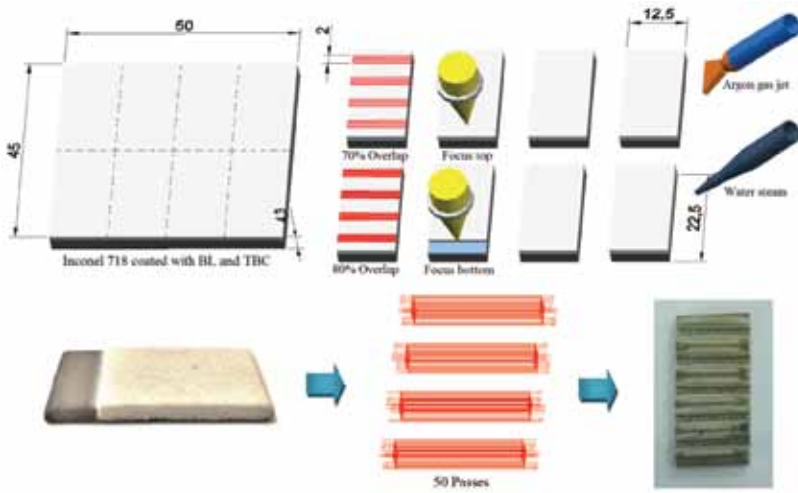


FIGURE 2

Laser removal of thermal barrier coating (TBC) of 1 mm thickness following 70 & 80% laser beam overlap, beam focus on top & bottom of the TBC layer, dry ablation, with assisting Argon gas jet, and with a low-pressure water steam jet. Clean tracks of 2 x 12.5 mm were obtained after 50 passes of the laser beam.

$$EC = \frac{P * t}{V_m} \quad (1)$$

Where EC is the energy consumption (J/mm^3), P is the average power (W), t is the total processing time (s), and V_m is the volume of material removed (mm^3).

2.3. Laser removal of the bond layer (BL)

Laser cleaning experiments were conducted on Inconel 718 coupons coated with bond layer (BL) coating $MgCrAlY$. High material removal rate and minimal thickness of the recast layer formed on top of the laser cleaned surface were targeted. The measured thickness of the BL coating was on average 350 μm . The laser beam was scanned on top of the BL to form a 2 x 12.5 mm clean track with a 70 % beam overlapping at four different power levels and under four different frequencies. Multiple preliminary tests have shown that higher material removal rates result when delivering the laser beam at high frequency; however, excessive melting develops which yields a non-uniform surface and left behind thick recast layers. On the other hand, delivering the laser at the low frequency generated flat uniform surfaces, but the material removal rates were very low and the heat input on the pieces was very high. Therefore, a novel laser removal process of this hard to process coating was implemented by applying two sets of laser scans. The first set was delivered

TABLE 4

Laser process conditions tested in the removal of bond layer - BL - (MCrAlY), following a two-step laser removal process. In the first step, the laser beam is scanned at high pulse frequency (≥ 8 kHz) with different number of passes (~ 215 passes). In the second step, laser beam is scanned at low frequency (6 kHz) with 100 passes.

No.	Beam overlap (%)	Focal point position (mm)	First removal step		Second removal step	
			Frequency (kHz)	Power level (W)	Frequency (kHz)	Power level (W)
1	70	0	8	315	6	315
2	70	0	8	360	6	315
3	70	0	8	405	6	315
4	70	0	8	450	6	315
5	70	0	10	315	6	315
6	70	0	10	360	6	315
7	70	0	10	405	6	315
8	70	0	10	450	6	315
9	70	0	12	315	6	315
10	70	0	12	360	6	315
11	70	0	12	405	6	315
12	70	0	12	450	6	315
13	70	0	14	315	6	315
14	70	0	14	360	6	315
15	70	0	14	405	6	315
16	70	0	14	450	6	315

at high frequency (≥ 8 kHz) which increased the material removal rate and the second delivers the laser beam at low frequency (6 kHz) which flattened the cleaning track and reduced the recast layer thickness.

In order to identify which combination of frequencies is ideal for the laser removal of this bonding layer a comprehensive experimental work was conducted. Here, two sets of laser beam scans were applied in each test. The first scan set comprised a large number of passes (on average 215) of the laser beam at four different frequencies i.e. 8,10,12 & 14 kHz, following four power levels (315, 360 405 & 450W) and under different traverse speeds and the number of laser scans. This initial set of passes at a high frequency removed the bulk of the BL coating material. A second scan set comprised 100 passes of the laser beam at 6 kHz frequency and average power of 315 W i.e. 70% of the power available in this laser system at this frequency. This secondary set of passes flattened the surface of the clean track and reduced the thickness of the recast layer as indicated above. Table 4 list the combina-

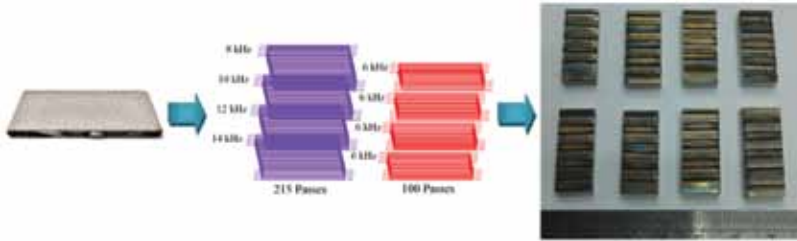


FIGURE 3

Laser removal of bond layer (BL) coating MCrAlY of 350 μm thickness at 70% laser beam overlap, focusing on top of the BL layer following two sets of laser scans, first a set of ~ 215 passes at different frequencies 8,10,12 & 14 kHz each followed by a second set of 100 passes at 6 kHz.

tion of process parameters tested for the removal of bond layer. A schematic of the laser removal procedure followed to remove the BL coating is shown in figure 3.

3. RESULTS

3.1. Beam overlap effect in laser removal of thermal barrier coating (TBC)

The laser cleaning of TBC with 80% beam overlapping produced clean tracks for the power levels and focal point positions tested under 50 passes of the laser beam. In contrast, at 70% laser beam overlap under the same process conditions did not completely remove the TBC coating. The consumption of energy per unit of volume of TBC removed was calculated for all the conditions tested in this experiment following equation 1. At 70% percent laser beam overlap, the effect of the focal point position on the energy consumption was minimal yielding only on average 1.64% lower energy consumption when the beam was focused at the bottom of the TBC coating as shown in figure 4 (b & d). The longer interaction time at 80% overlapping condition yielded higher energy consumption. A similar trend was observed when increasing the power applied in the removal process. Here, the laser beam focused at the bottom of the TBC layer improved on average 6.33% the energy consumption efficiency as shown in figure 4 (a & c). This, as the laser beam is converging along the depth of the TBC coating layer, which maximises the removal of material in the laser cleaning process.

3.2. Beam focal point location and assisting media effect in laser removal of thermal barrier coating (TBC)

The effect of focusing the laser beam on the top and bottom of the TBC coating layer was investigated for a laser beam overlapping of 75% at different power

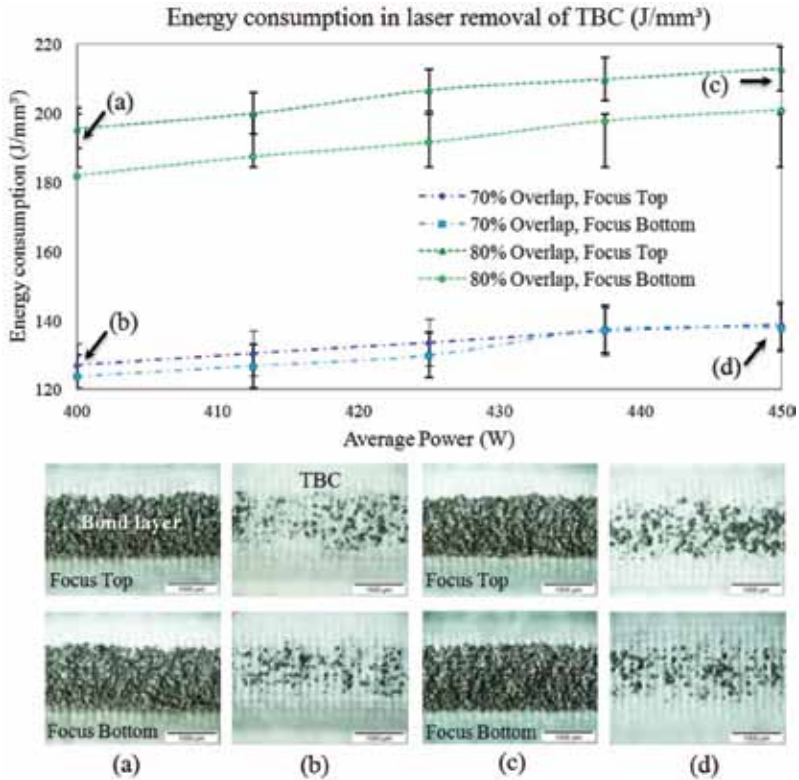


FIGURE 4

Calculated energy consumption in the laser cleaning of TBC at different beam overlapping conditions, power level, and focal point positions. Clean tracks were obtained at 80% beam overlapping at 400W (a) and 450W (c) power levels. Tests at 70% beam overlap showed remnants of TBC coating at 400 W (b) and 450 W (d) power levels.

levels in a definitely manner. Since the two previous conditions tested resulted in excessive removal (80% overlap) or incomplete removal (70% overlap) of the TBC coating layer. Furthermore, the effects of assisting media in the laser cleaning process were explored for the focal point position at the bottom of the TBC coating layer. In particular, the shear stress produced by an assisting side Argon knife gas jet at 2 bars of pressure with an incident angle of $\sim 25^\circ$ and the explosive ejection of steam water while in interaction with the laser beam were investigated. In these experiments, five different power levels were employed, while maintaining constant the scanning speed of 975 mm/s, the overlapping of the scanned lines was set at 75%, and the number of passes at 50 for each condition (see Table 3 tests 21-40). The energy consumption per unit of volume in laser cleaning of TBC for each condition tested was calculated following equation 1. A graphical overview of the results obtained in this experiment is presented in figure 5. The effect of the beam focal point position was clearly observed at a 400W

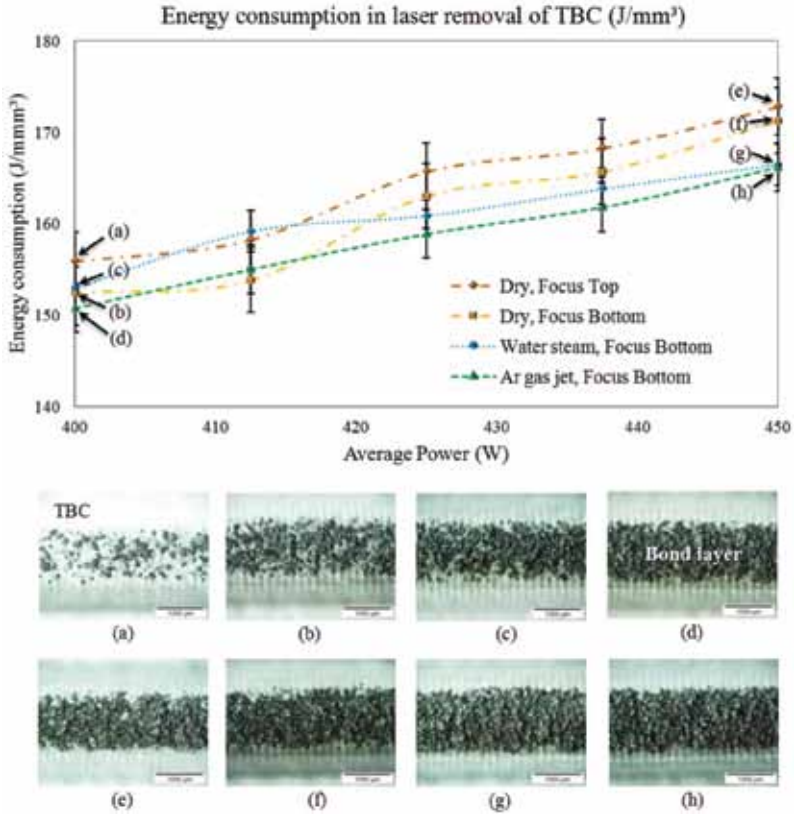


FIGURE 5
 Calculated energy consumption in the laser cleaning of TBC at 75 % overlapping and at different focal point positions and assisting media. Dry TBC with laser beam focused on top at 400W (a) and 450W (e); Dry TBC with laser beam focused at the bottom at 400W (b) and 450W (f); Water steam with laser beam focused at the bottom at 400W (c) and 450W (g); Argon gas jet with laser beam focused at the bottom at 400W(d) and 450W (h).

power level at the dry condition which generated cleaner tracks when focusing at the bottom figure 5(b) as compared to focussing at the top figure 5(a). In general, higher power level produced clean tracks as seen in figure 5 (e - h), while the action of the Argon gas jet figure 5(d) and low-pressure water steam figure 5(c) helped to obtain cleaner tracks than those obtained by the laser beam alone -dry condition- figure 5(b). High power level, however, increased the amount of energy consumed per unit volume as shown in the graph in figure 5.

3.3. Laser removal of bond layer

Multiple experiments were conducted at each of the 16 combinations matching four power levels (315, 360 405 & 450W) with four pulse frequencies (8,

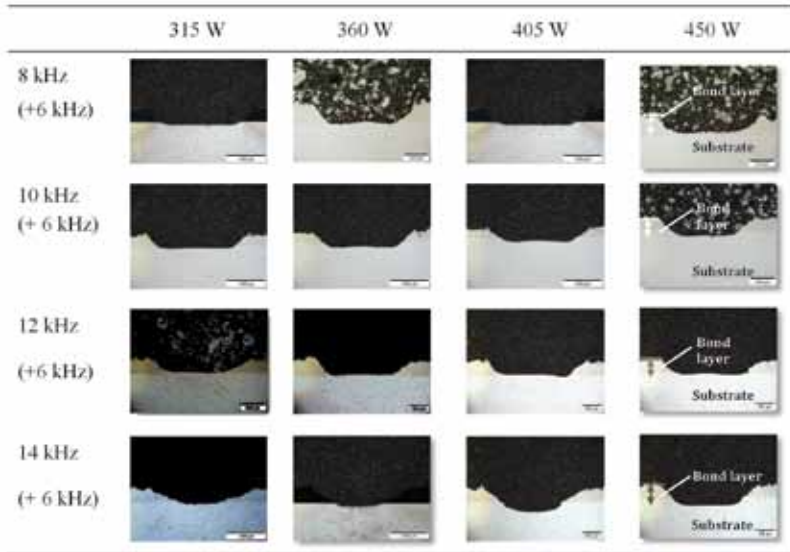


FIGURE 6

Laser removal of the bond layer by two sets of scanning patterns (two different frequencies) with 70 % overlapping of the laser beam and different power levels, traverse speed and number of passes.

10, 12 & 14 kHz) to reach the substrate with flat surfaces, avoiding cracks and obtaining thin recast layers (see Table 4). The traverse speed and number of laser beam passes were adjusted to obtain clean pieces with these combinations of pulse frequencies. Figure 6 shows the cross-section of the BL laser removal results for all the combinations investigated. The samples show that the BL was completely removed where the laser beam reached the substrate and the cleaned tracks had fairly flat surfaces.

The material removal rate was measured for each parameter combination. The thickness of the recast layer left on the surface after the laser stripping of the BL for each condition was measured by optical microscopy. Figure 7 shows both the computed material rate and the thicknesses of the recast layer measured after the laser stripping process for all the conditions. The recast layer thicknesses recorded were below 5 μm in all conditions.

The experimental results show that low frequencies of 8 & 10 kHz, at similar power levels, yielded lower material removal rates as compared to higher frequencies of 12 & 14 kHz, which improved the rate of material removal. The second laser beam scan set of 100 passes at 315W average power and 6 kHz pulse frequency which yields higher peak power. This second scan flattens the treated surface by the laser beam. The high peak power ablates the material uniformly; however, the material removal rate is low and the heat input is high.

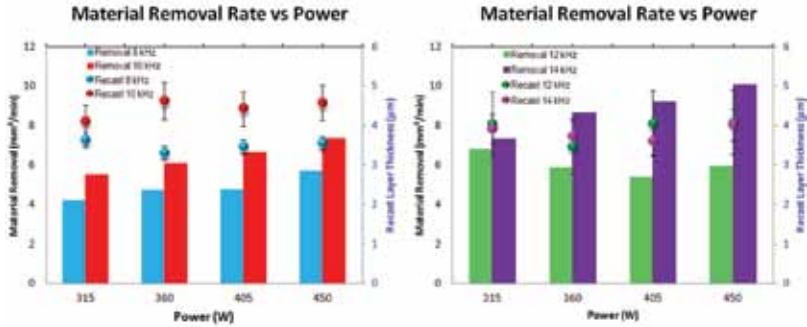


FIGURE 7 Material removal rate and recast layer thickness in the laser removal of BL (MCrAlY) by two scanning sets at different frequencies.

3.4. WDS Analysis of laser cleaned surfaces

A Wavelength-Dispersive X-Ray Spectroscopy (WDS) analysis of the laser stripped surfaces was conducted to determine the oxygen content after the cleaning process (reduction or avoidance of oxidation effects). The analysis was conducted on the cross section of the laser treated surfaces. The WDS analysis reveals the chemical composition of the recast layer and the substrate material Inconel 718 for the complete experimental matrix on BL laser cleaning. The analysis identified the proportion of the main elements present in Inconel 718 and the bond layer coating MCrAlY. Here, twelve elements were analysed at four points in each recast layer cross section. Furthermore, two points on the base material for half of the treatments were analysed as shown in Figure 8. The best results obtained in terms of low levels of Oxygen were obtained when cleaning with laser frequencies of 8 and 14 kHz. Table 5 shows the elements detected by the WDS analysis of this selected laser cleaned surfaces. The second condition at 14 kHz is beneficial for this process as it resulted in higher removal rates of the bond layer.

3.5. XRD Analysis

An X-ray diffraction (XRD) analysis was conducted to identify the residual stresses present in laser cleaned surfaces. This technique has been employed by various groups to investigate the degree of change to the residual stresses in the sample after subjecting the sample to TBC depositions and cyclic thermal treatments [28-31]. The residual stress analysis was conducted with an X-ray diffractometer following the $\cos\alpha$ method. The diffractometer employs a Chromium X-ray source. The scanning angle was fixed at 35° , while X-rays were collimated by a 1mm point collimator. Four measurements were taken from the sample surface, each point located 3 mm apart. Figure 9 shows the set up employed for this analysis. The results indicated that tensile stresses

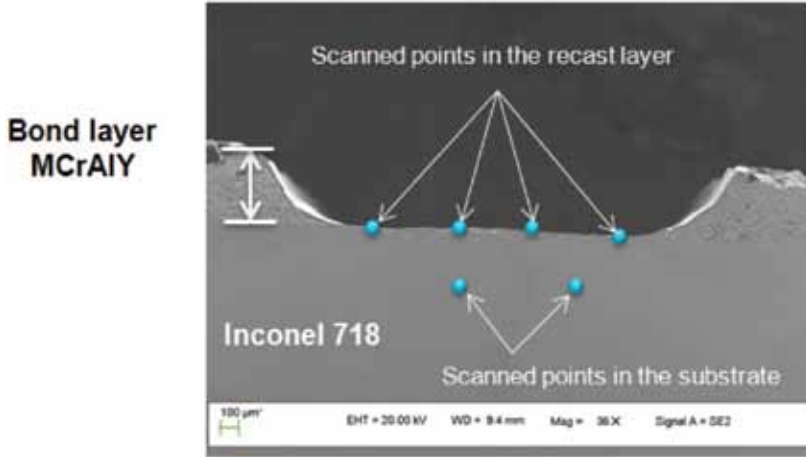


FIGURE 8
WDS analysis conducted at four locations on the recast layer cross-section and at two locations on the substrate.

TABLE 5
Selected WDS results of laser cleaned surfaces at 8 and 14 kHz.

FREQ	Element (weight %)	Recast layer				Inconel 718	
		315 W	360 W	405 W	450 W	360 W	405 W
8 kHz (+ 6 kHz)	Ni	55.56	51.74	50.66	54.91	50.81	50.63
	Co	2.77	2.11	0.79	1.25	0.43	0.40
	Fe	19.15	18.24	18.28	19.09	18.64	18.66
	Cr	12.93	13.16	14.00	10.85	17.86	18.25
	Mo	2.30	2.42	2.48	2.37	2.91	2.23
	O	1.21	1.17	2.29	1.79	0.84	0.89
	Al	0.85	1.14	1.00	1.00	1.64	1.70
14 kHz (+ 6 kHz)	Ni	50.97	49.83	52.23	51.72	50.94	50.48
	Co	0.70	1.43	1.70	5.53	0.36	0.38
	Fe	17.50	16.69	17.26	16.12	18.55	18.29
	Cr	9.94	10.69	9.99	10.26	18.21	18.25
	Mo	3.57	3.15	3.23	2.50	2.86	2.80
	O	3.15	2.81	2.99	2.01	0.79	0.74
	Al	0.91	1.74	1.30	1.74	1.77	1.77

were present on the surface of the laser cleaned samples as shown in Table 6, with an average value of 547 MPa. Conversely, compressive stresses of an average value of -264 MPa were measured from the surface of a pristine cou-

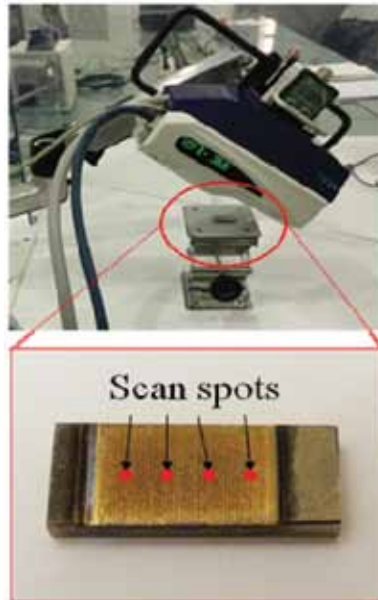


FIGURE 9
Set-up for XRD analysis of a laser treated Inconel 718.

TABLE 6
Residual stress (MPa) measurements of Inconel 718, Inconel 718 coated with BL and TBC and a laser ablated Inconel 718.

Inconel 718	Inconel + BL + TBC	Laser cleaned Inconel 718
-358	975	347.2
-154	269	456
-361	302	921.2
-183	706	465.5

pon. Finally, tensile stresses of an average value of 563 MPa were measured from samples subjected to TBC coating process conditions. This residual stresses balance between the substrate/coating compound results from quenching stresses and the coefficient of thermal expansion (CTE) mismatch stress [28-32]. The former develops when the melted TBC coating (Yttria-stabilised zirconia) rapidly solidifies and cools over the substrate material (Inconel 718 + BL) [28, 29]. The latter -CTE- results from the thermal expansion mismatch between the coating materials and the substrates [30, 31]. The similar average values of residual stresses obtained from both the TBC coated and the laser cleaned samples suggest that the laser cleaning process does not

induce significant changes to the surface residual stress profile of the sample. Tensile stresses were expected on this process as the Inconel 718 substrates were heated by the laser removal process which then follows a cooling process. These phenomena have been reported on laser additive processes [33].

4. DISCUSSION

4.1. Laser removal of the thermal barrier coating

From the experimental evidence reported herein, it was observed that the focal point position at the bottom of the TBC coating yielded cleaner tracks as the laser beam converges along the thickness of the coating. Here, the power density continuously increases given the smaller beam spot sizes. The opposite effect is observed when the focal point position is located at the top of the TBC i.e. the laser beam starts to diverge as it propagates along its thickness. Furthermore, the consumption of energy was better optimised when the laser beam was located at the bottom of the TBC coating layer.

The use of assisting Argon gas jet helped to clean tracks and to reduce the energy consumption see figure 5 (d & h). This by ejecting more material from the processing area given the shear stress applied to it, this clearing effect also enhances the laser-material interaction. Furthermore, water steam also reduced the energy consumption per unit of material removed. This by expelling more material from the cleaned surfaces through an explosive boiling effect produced when the low-pressure water steam jet interacts with the high-power infrared laser beam. Optimal removal conditions were power level 400 - 450W, laser beam overlap of 75%, focus at the bottom of the TBC layer, 50 passes and 975 mm/s traverse speed. These conditions yielded clean traces with average removal rates of 140 mm³/min.

A novel two-step laser scanning process removed the BL (MCrAlY) coating which is a very tough interface protective layer for the Inconel 718 alloy. This layer proved difficult to be removed by a single set of parameters, therefore a suitable method has been developed. The combination of different scanning sets proved effective for the laser cleaning process of the BL coating. Here, the scanning of the laser beam at high pulse frequencies improves the removal rate of the material. The application of a second scanning set, i.e. laser beam delivered at low frequency and high-power level (high peak power), flattened the surface of the laser cleaned sample and yielded thinner recast layer. This layer cannot be fully avoided as the thermal nature of the nanosecond laser removal process; nonetheless, it was minimised as it was below 5 µm in thickness in all conditions. The optimal condition identified was a set of 170 passes at 14 kHz frequency and 450W (100% of power level available). This was followed by a set of 100 passes at 6 kHz and 315W yielding a material removal rate of 10 mm³/min and recast layer of 4 µm.

A WDS analysis was employed to identify the chemical composition of laser cleaned surfaces for the complete set of conditions tested. Since the laser removal process is conducted in an open-air environment and under high power level condition, the Nickel based alloy is susceptible to oxidation. It is important to minimise any oxidation as Inconel 718 is employed in the manufacture of valuable elements such as aero-engine and power turbine components. In particular, serviced aero-engine components follow a series of repairs and coating steps after the cleaning process of TBC and BL; therefore, oxidation levels shall be minimised. Results from WDS analysed laser treated materials showed that low oxidation levels were attained in pieces cleaned by the laser beam scanned at 8 kHz and at 14 kHz followed by 6 kHz scanning step. The latter combination i.e. 14 kHz followed by 6 kHz laser beam scans at 400W power level was the optimal condition as it yielded higher removal rate of the material.

5. CONCLUSIONS

A laser removal process of TBC was conducted with a high power Nd:YAG pulsed laser. Clean tracks were obtained at 75 & 80% overlapping of the top-hat and 600 μm square laser beam employed. The efficiency of the laser cleaning process improved when the focus was located at the bottom of the TBC coating as the laser beam converges along its thickness. The assisting media, Argon gas jet and low-pressure steam water, improved the material removal rate in the TBC laser cleaning process which in turn reduced the consumption of energy.

A novel two step laser removal process of the bond layer (MCrAlY) has been developed. The first step delivered multiple passes of the laser beam at high pulse frequency (14 kHz) which achieved high material removal rate. The second step consisted of a set of multiple passes of the laser beam at low pulse frequency which flattened the cleaned sample surface and yielded thinner recast layer.

WDS analysis was employed to identify oxidation levels on BL laser cleaned samples. A laser removal process with 170 passes of the laser beam at pulse frequency of 14 kHz at 450W, followed by 100 passes of the laser beam at pulse frequency of 6 kHz at 315W was found as optimal condition as it yielded higher material removal rate with low oxidation at the surface.

XRD analysis helped to identify the type and magnitude of residual stresses after the laser cleaning process. Their measured residual stresses are tensile in nature with an average magnitude of 547 MPa, which were comparable in magnitude to the tensile stresses from samples subjected to the TBC coating process at 563 MPa. The pristine Inconel 718 coupons had compressive residual stress with average value of -264 MPa.

REFERENCES

- [1] Guan Y.C., Ng G. K. L., Zheng H. Y., Hong M. H., Hong M.H., Hong X. and Zhang Z. Laser surface cleaning of carbonaceous deposits on diesel engine piston. *Applied Surface Science* **270** (2013), 526-530.
- [2] Wang X. and Zheng H. Picosecond laser micro-drilling, engraving and surface texturing of tungsten carbide. *Journal of Laser Applications* **30** (2018), 032203.
- [3] Wang X.C., Wang B., Xie H., Zheng H.Y. and Lam Y.C. Picosecond laser micro/nano surface texturing of nickel for superhydrophobicity. *Journal of Physics D: Applied Physics* **51** (2018), 115305.
- [4] Lu L., Zhang Z., Guan Y. and Zheng H. Comparison of the effect of typical patterns on friction and wear properties of chromium alloy prepared by laser surface texturing. *Optics & Laser Technology* **106** (2018), 272-279.
- [5] Turner M.W., Crouse P.L. and Li L. Comparison of mechanisms and effects of Nd:YAG and CO₂ laser cleaning of titanium alloys. *Applied Surface Science* **252** (2006), 4792-4797.
- [6] Turner M.W., Crouse P., Li L. and Smith A. J. E. Investigation into CO₂ laser cleaning of titanium alloys for gas-turbine component manufacture. *Applied Surface Science* **252** (2006), p. 4798-4802.
- [7] Turner M.W., Crouse P. and Li L. Comparative interaction mechanisms for different laser systems with selected materials on titanium alloys. *Applied Surface Science* **253** (2007), 7992-7997.
- [8] Whitehead D.J., Crouse P.L., Schmidt M.J.J., Li L., Turner M.W. and Smith A.J.E. Monitoring laser cleaning of titanium alloys by probe beam reflection and emission spectroscopy. *Applied Physics A* **93** (2008), 123-127.
- [9] Dahl K.V., Hald J. and Horsewell A. Interdiffusion between Ni-based superalloy and MCrAlY coating. *Defect and Diffusion Forum* **258-260** (2006), 73-78.
- [10] Sezer H.K., Pinkerton A.J. and Li L. An investigation into delamination mechanisms in inclined laser drilling of thermal barrier coated aerospace superalloys. *Journal of Laser Applications* **17** (2005), 225-234.
- [11] Sezer H.K., Li L., Schmidt M., Pinkerton A.J., Anderson B. and Williams P. Effect of beam angle on HAZ, recast and oxide layer characteristics in laser drilling of TBC nickel superalloys. *Machine Tools & Manufacture* **46** (2006), 1972-1982.
- [12] Sezer H.K., Li L. and Leigh S. Twin gas jet-assisted laser drilling through thermal barrier-coated nickel alloy substrates. *International Journal of Machine Tools & Manufacture* **49** (2009), 1126-1135.
- [13] Feng Q., Picard Y., McDonald J. P., Rompay V.P.A., Steven Y. and Pollock T. M. Femto-second laser machining of single-crystal superalloys through thermal barrier coatings. *Materials Science and Engineering A* **430** (2006), 203-207.
- [14] Jia Q. and Gu D. Selective laser melting additive manufacturing of Inconel 718 superalloy parts: Densification, microstructure and properties. *Journal of Alloys and Compounds* **585** (2014), 713-721.
- [15] Wang D., Tian Z., Shen L., Liu Z. and Huang Y. Effects of laser remelting on microstructure and solid particle erosion characteristics of ZrO₂-7wt% Y₂O₃ thermal barrier coating prepared by plasma spraying. *Ceramics International* **40** (2014), 8791 - 8799.
- [16] Bennetta J. L., Kafka O. L., Liao H., Wolff S. J., Yu C. Cheng P. Hyatt G. Ehmann K. Cao J. Cooling rate effect on tensile strength of laser deposited Inconel 718. *Procedia Manufacturing* **26** (2018), 912-919.
- [17] Sui S., Chen J., Ma L., Fan W., Tan H., Liu F. and Lin X. Microstructures and stress rupture properties of pulse laser repaired Inconel 718 superalloy after different heat treatments. *Journal of Alloys and Compounds* **770** (2019), 125-135.
- [18] Helmick D.A. and Burin D.L. Thermal barrier coating removal via shockwaves stresses, *T.U.S.P.a.T. Office*, Editor. 2010, General Electric Company: USA. 4.

- [19] Helmick D.A. and Burin D. A. Method and system for removing thermal barrier coating, *T.U.S.P.a.T. Office, Editor*. 2010, General Electric Company: USA. 6.
- [20] Thompson C.E. Water jet stripping and recontouring of gas turbine buckets and blades, *T.U.S.P.a.T. Office*, General Electric Company: USA. 13.
- [21] Miller M.O., Pearson W. R. and Thompson W. R. Method and apparatus for removing coatings from a substrate using multiple sequential steps, *T.U.S.P.a.T. Office*, Editor. 2011, Huffman Corporation: USA. 9.
- [22] Thompson W.R. Method and apparatus for selectively removing portions of an abradable coating using a water jet, *T.U.S.P.a.T. Office, Editor*. 2010, Huffman Corporation: USA. 9.
- [23] Marimuthu S., Kamara A. M., Sezer H., Li L. and Ng G.K.L. Numerical investigation on laser stripping of thermal barrier coating. *Computational Materials Science* **88** (2014), p8.
- [24] Wolf K. Laser Strip: A Portable Hand-Held Laser Stripping Device for Reducing VOC, *Toxic and Particulate Emissions*. 2009: California, USA. 129.
- [25] Li L., Spencer J. T. and Key P. H. A comparative study of the effects of laser wavelength on laser removal of chlorinated rubber. *Applied Surface Science* **138-139** (1999), 418-423.
- [26] Razab M.K.A.A., Noor A.M., Jaafar S.M., Abdullah N. H., Suhaimi F.M., Mohamed M., Adam N., Alnur N. and Yusuf A. N. A review of incorporating Nd:YAG laser cleaning principal in automotive industry. *Journal of Radiation Research and Applied Sciences* **11**(4) (2018), 393 - 402.
- [27] Jaeschke P. Laser cutting for carbon fiber-reinforced composite structures, in *Industrial Laser Solutions for Manufacturing*. PennWell: Nashua, NH, USA. 28.
- [28] Levit M., Grimberg I., and Weiss B. Z. Residual stresses in ceramic plasma-sprayed thermal barrier coatings: measurement and calculation. *Material Science and Engineering* **A206** (1996), 30-38.
- [29] Kesler O., Matejicek J., Sampath S., Suresh S., Gnaeupel-Herold T., Brand P.C. and Prask H. J. Measurement of residual stress in plasma-sprayed metallic, ceramic and composite coatings. *Materials Science and Engineering* **A257** (1998), 215-224.
- [30] Teixeira V., Andritschky M., Fischer W., Buchkremer H.P.D. and Stöver D. Effects of deposition temperature and thermal cycling on residual stress state in zirconia-based thermal barrier coatings. *Surface and Coatings Technology* **120-121** (1999), 103-111.
- [31] Teixeira V., Andritschky M., Fischer W., Buchkremer H.P.D. and Stöver D. Analysis of residual stresses in thermal barrier coatings. *Journal of Materials Processing Technology* **92-93** (1999), 209-216.
- [32] Swank W.D., Gavalya R.A., Wright J.K. and Wright R.N. Residual Stress Determination from a Laser-Based Curvature Measurement, in *Thermal Spray 2000: Surface Engineering via Applied Research*, C.C. Berndt, Editor. ASM International: Montreal, Quebec, Canada. 2000, p. 7.
- [33] Kamara A.M., Marimuthu S. and Li L. A numerical Investigation into residual stress characteristics in laser deposited multiple layer waspaloy parts. *Journal of Manufacturing Science and Engineering* **133** (2011), 031013-1 - 9.

Evaluation of Surface Properties of Silicon Nitride Ceramics Treated with Laser Peening

K. SAIGUSA¹, K. TAKAHASHI^{1*} AND N. SIBUYA²

¹*Faculty of Engineering, Yokohama National University, 79-5 Tokiwadai,
Hodogaya-ku, Yokohama-shi, Kanagawa, Japan*

²*Sintokogio, LTD, 71-2 Tsukeda, Nishijo, Oharu-cho, Ama-gun, Aichi, Japan*

Laser peening (LP) is a process that has been mainly applied to metals. However, few studies have applied LP to ceramics. In this study, laser peening without coating (LPwC) was applied to silicon nitride reinforced with silicon carbide ($\text{Si}_3\text{N}_4/\text{SiC}$). Smooth, laser-peened, and shot-peened specimens were prepared, and the surface conditions, surface roughness, and residual stresses were investigated. The surface roughness increased after LP due to laser ablation. When the LP parameters such as power density and coverage were too high, cracks initiated on the surface. Further, when appropriate LP parameters were selected, a compressive residual stress of up to 230 MPa was introduced on the surface and the depth was about 50 μm . Although the magnitude of the surface residual stress of the laser-peened specimen was smaller than that of the shot-peened specimen, LP was able to introduce a deeper compressive residual stress.

Keywords: Laser peening, silicon nitride, ceramics, residual stress, surface roughness, surface properties

1 INTRODUCTION

Ceramics have excellent properties compared to metals, such as heat shock resistance, ablation resistance, and corrosion resistance. Therefore, ceramics are used in various applications. However, ceramic materials are brittle. Thus, their fracture toughness is much lower than that of metals.

To address this problem, many studies have been conducted with the goal of increasing the strength of ceramics by controlling their microstructures

Corresponding author's e-mail: takahashi-koji-ph@ynu.ac.jp

and developing composite materials. In addition, surface treatments have also been studied. Shot peening (SP) is a technique used to introduce compressive residual stress by hitting small shot materials against the surface of the target material. In recent years, the effects of SP on ceramics have been studied by several researchers [1–8]. Ito *et al.* reported that the bending strength of partially stabilized zirconia (PSZ) increased after SP [1]. Moon *et al.* reported that a compressive residual stress was introduced by SP on the surface of silicon nitride, which improved the apparent fracture toughness [2]. Tanaka *et al.* reported that a compressive residual stress was introduced in silicon nitride by fine-particle peening and ultrasonic peening, resulting in improved apparent fracture toughness [3]. Pfeiffer *et al.* also reported that the compressive residual stress introduced by SP increased the static and cyclic load capacities of alumina and silicon nitride [4]. Takahashi *et al.* reported that improvements in the apparent fracture toughness and contact strength of a $\text{Si}_3\text{N}_4/\text{SiC}$ composite material were achieved by SP [5]. Takahashi *et al.* also showed that the bending strength and abrasion resistance of PSZ increased due to the effects of the compressive residual stress induced by SP [6, 7]. Shukla reported that the surface fracture toughness of a zirconia-advanced ceramic increased by micro-shot peening [8]. However, due to the physical contact with the shot material during SP, there is a possibility of surface peeling or chipping, which can result in large decreases in strength.

Therefore, we focused on laser peening (LP) in this study. LP is a technique that utilizes the impact force of plasma generated by the irradiation of a pulsed laser. LP is used for preventing many forms of damage, such as fatigue, wear, and stress corrosion cracking (SCC) in metals. For example, introduction of residual stress and improvement of the fatigue performances of metal components by LP were reported [9]. Sano *et al.* investigated the residual stress improvement in the surface of SUS304 by laser irradiation [10]. In addition, the application of LP to various materials has been studied. For example, retardation of crack initiation in austenitic stainless steels [11] and improvement in the fatigue life of a titanium alloy [12] were reported. Moreover, stress corrosion cracking resistance and significant decreases in fatigue crack growth rates in aluminum alloy welded joints were reported [13, 14]. Further, introduction of residual stress and improvement of the fatigue strength of a nickel-based alloy were reported [15].

Further, the effects of LP on ceramics have been studied as follows. Akita *et al.* reported that compressive residual stresses up to 270 MPa could be introduced by applying LP to silicon nitride. They also reported that the bending strengths of laser-peened specimens were improved compared to those of smooth specimens [16]. Shukla *et al.* reported that LP improved the hardness and fracture toughness of alumina [17] and silicon carbide [18], and that compressive residual stresses were introduced to Al_2O_3 armor ceramics [19]. In addition, Shukla and Lawrence applied LP to Si_3N_4 advanced ceramics and reported an improvement in fracture toughness [20, 21]. Shukla sum-

marized the results of LP of ceramics in recent years [22]. Wang et al. applied LP to Al_2O_3 ceramics and reported that compressive residual stresses of up to 671 MPa were introduced on the surface with a depth of about 1.2 mm [23]. Wang et al. also reported that compressive residual stresses of 850–900 MPa were generated on the surface of Al_2O_3 ceramics by LP, and were retained on the surface after annealing for 10 h at 1100 °C and 1300 °C [24]. Xing et al. found that femtosecond LP improved the wear resistance of $\text{Al}_2\text{O}_3/\text{TiC}$ cutting tools [25].

As mentioned above, many studies have applied LP to metals. However, the application of LP to ceramics has been limited because of the concerns regarding the formation of micro-cracks under the strong LP conditions required to introduce large compressive residual stresses. Therefore, when LP is applied to ceramics, it is necessary to investigate the relationship between LP and the surface conditions.

In this study, we applied LP to silicon nitride reinforced with silicon carbide ($\text{Si}_3\text{N}_4/\text{SiC}$) and investigated its surface properties such as the surface roughness and residual stress distribution. Finally, we determined the appropriate LP conditions for $\text{Si}_3\text{N}_4/\text{SiC}$.

2 EXPERIMENTAL PROCEDURES

2.1 Materials and specimens

In this study, we used silicon nitride reinforced with silicon carbide ($\text{Si}_3\text{N}_4/\text{SiC}$). The samples were prepared using a mixture of Si_3N_4 with 20 wt% SiC powder and 8 wt% Y_2O_3 as a sintering additive. The mixed powders were dried and subsequently hot-pressed at 1850 °C and 35 MPa for 2 h in a N_2 atmosphere. Detailed methods for preparing the test materials were reported previously [26]. The hot-pressed plates were then cut into test specimens measuring 3 mm × 4 mm × 40 mm. One face of each specimen was ground with a grindstone and polished with a 6 μm diamond slurry to a mirror-like finish. The arithmetic average surface roughness (R_a) was 0.025 μm. One of the edges of the specimen was chamfered. This specimen is denoted as the “smooth specimen.”

2.2 Laser peening process

Laser peening without coating (LPwC) was applied to the smooth specimens in water. Table 1 lists the conditions of the LP process. The second harmonic of a Q-switched Nd:YAG laser ($\lambda = 532$ nm, SAGA, Thales, France) was used. The pulse duration (t) was 6.2 ns and the repetition rate was 10 Hz. The spot diameter of the laser (D) was fixed as 0.5 mm. The pulse energy (E_p) indicates the energy contained per pulse of the laser. The irradiation density (N_p) indicates the number of pulses irradiated per unit area. The peak power

TABLE 1
Conditions of laser peening.

Specimens	Pulse energy, E_p [mJ]	Spot diameter, D [mm]	Power density, G [GW/cm ²]	Irradiation density, N_p [Pulse/mm ²]	Overlap-ping pitch [mm]	Overlap ratio [%]	Coverage, C_v [%]
Specimen 1	24		2	16	0.25	50	314
				51	0.14	72	1000
				153	0.081	84	3000
				255	0.063	87	5000
Specimen 2	194	0.5	16	16	0.25	50	314
				51	0.14	72	1000
				153	0.081	84	3000
				255	0.063	87	5000
Specimen 3	401		33	16	0.25	50	314
				51	0.14	72	1000
				153	0.081	84	3000
				255	0.063	87	5000

density (G), which is the light intensity per unit area, can be calculated by the following equation using the pulse energy, E_p , and spot area, A_p ($= \pi d^2/4$):

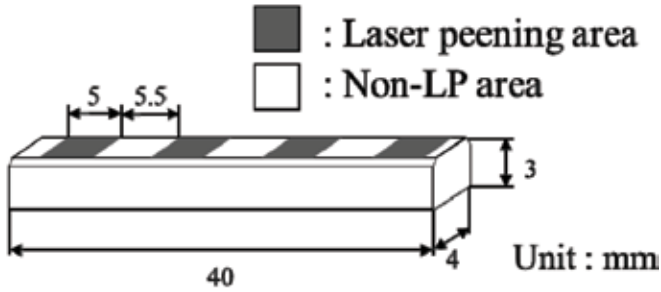
$$G = \frac{E_p}{A_p t} \quad (1)$$

Three power densities, $G = 2, 16, \text{ and } 33 \text{ GW/cm}^2$, were selected.

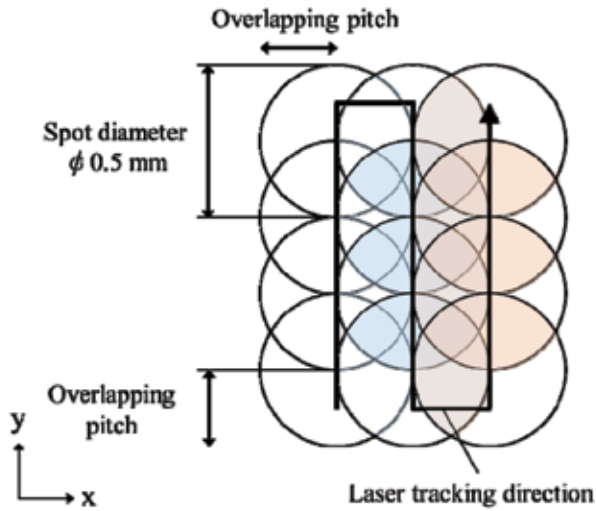
Figure 1(a) shows the peening area of the specimen, and Figure 1(b) shows the peening pattern and laser track in the laser-peened area. Figure 1(c) shows the experimental setup of LP. The specimens were submerged in a water bath, and then processed by LP. The laser was rastered over the specimens in the y (width) direction followed by shifting in the x (longitudinal) direction in one layer. The pitches of the laser spot were ranged from 0.063 to 0.25 mm, and the corresponding overlap ratios were 50% to 87%. The pitch is the distance between two laser-irradiated spots. In Figure 1(c), the pitch in the x direction is the same as the pitch in the y direction.

The coverage, C_v , which is the amount of overlap per unit area, is calculated by the following equation proposed by Sano et al. [10] using the irradiation density, N_p , and spot area, A_p :

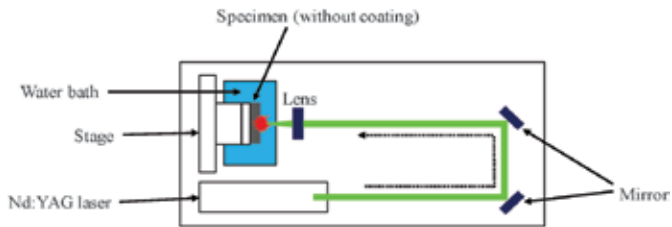
$$C_v = N_p A_p \quad (2)$$



(a) Laser peening area of the specimen



(b) Peening pattern and laser track in the laser peening area



(c) Experimental setup of laser peening

FIGURE 1
Schematic diagram of peening method applied to the specimen.

Here, $C_v = 314, 1000, 3000,$ and 5000% were selected. In this LP, we constructed 1 path. In this study, shot-peened specimens were also prepared for comparison. In SP, the shot diameter was $300\ \mu\text{m}$ and the shot pressure was $0.2\ \text{MPa}$ [5].

2.3 Measurement of surface condition, surface roughness, and residual stress

Surface observations and surface roughness measurements of the specimens were carried out using an optical microscope and a stylus-type surface roughness-measuring machine, respectively. For the surface roughness measurements, three random points on the surface of each test specimen were measured in the longitudinal direction, and an average value was calculated. The R_a was used as a parameter for the surface roughness.

In addition, the surface residual stresses of the laser-peened specimens in the longitudinal direction were measured by the $\cos\ \alpha$ method using an X-ray residual stress-measuring device. The residual stress was evaluated at three points and an average was calculated. In this study, the (212) diffraction peak of Si_3N_4 was measured using the Cr-K α characteristic X-ray line.

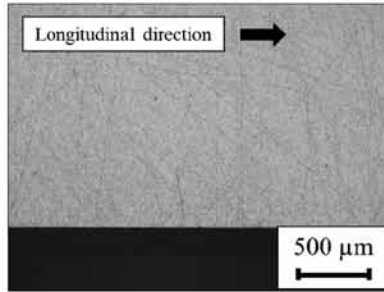
Furthermore, to evaluate the residual stress distribution in the depth direction, sequential polishing in the depth direction was performed. During polishing, the surface of the specimen was mirror-finished by buffing with a diamond slurry with a particle diameter of $1\ \mu\text{m}$. The amount of polishing was measured based on the change in the thickness of the specimens before and after polishing using a micrometer.

3 RESULTS AND DISCUSSION

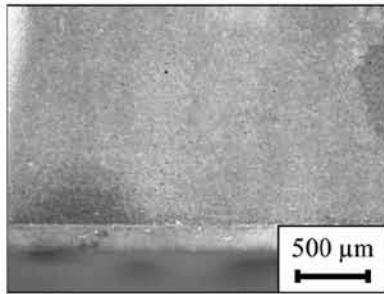
3.1 Surface observations and surface roughness

The surface of each test specimen was observed. Figure 2 shows the optical micrographs of the surface of each specimen. There was no chipping on the edge of the smooth specimens, as shown in Figure 2(a). The micrographs in Figure 2(b) and (c) show an enlarged view of the surface on which LP was applied. The specimens that were laser peened with a power density of $16\ \text{GW}/\text{cm}^2$ and coverage of 1000% exhibited a partially dark and discolored surface, while the edges remained similar to that of the smooth specimens, as shown in Figure 2(b). However, surface cracks were observed on the surface of the samples laser peened with a power density of $16\ \text{GW}/\text{cm}^2$ or more and coverage of 3000% or more, as shown in Figure 2(c). Chipping and peeling were clearly observed at the edges of the shot-peened specimens due to the physical contact of the shot material, as shown in Figure 2(d).

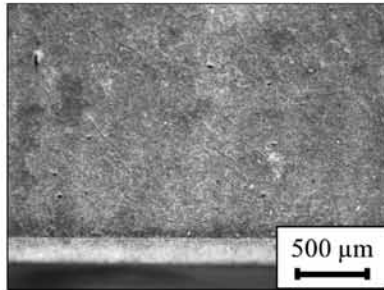
Figure 3 shows the calculated R_a of each test specimen. The R_a of the laser-peened specimens increased with increasing coverage and power density. The asterisk mark in Figure 3 shows that surface cracks occurred due to LP.



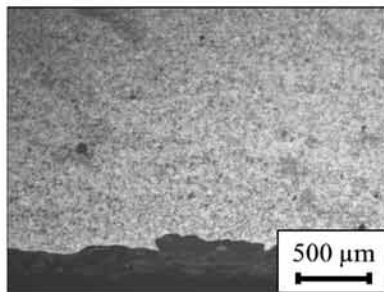
(a) Smooth (Non-LP) specimen



(b) Laser-peened specimen
($G = 16 \text{ GW/cm}^2$, $C_v = 1000\%$)



(c) Laser-peened specimen



(d) Shot-peened specimen
($G = 16 \text{ GW/cm}^2$, $C_v = 3000\%$)

FIGURE 2
Optical micrographs of the surfaces of the specimens.

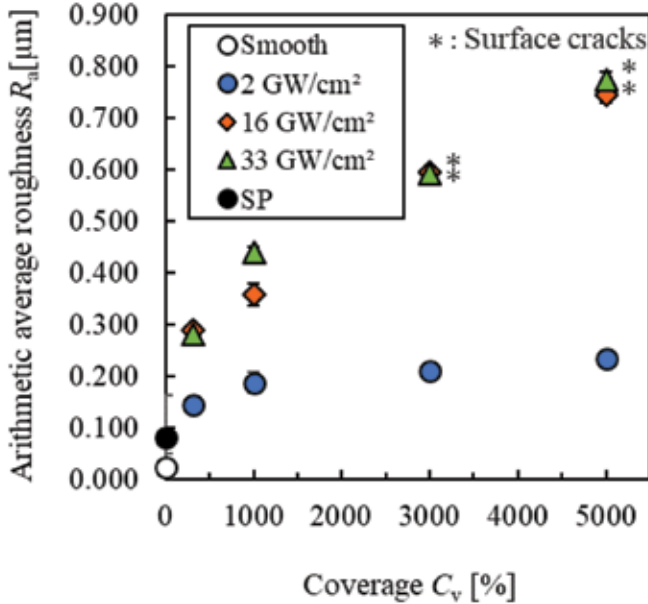


FIGURE 3
Surface roughness (R_a) of each surface-treated specimen.

3.2 Surface residual stress

Figure 4 shows the residual stresses measured at the surfaces of the specimens. Compressive residual stress was introduced by LP. The maximum compressive residual stress was about 280 MPa. The specimens that were laser peened at 16 and 33 GW/cm² showed much larger compressive residual stresses than those peened at 2 GW/cm². The asterisk mark in Figure 4 shows the occurrence of surface cracks. Surface cracks were observed on the sample when the LP parameters such as power density and coverage were too high.

3.3 Residual stress distribution from the surface in the depth direction

Figure 5 shows the residual stress distribution for each coverage. Generally, the compressive residual stress and the depth of the crossing point (i.e., the point at which the residual stress changes from compression to tension) tend to increase as the value of G increases. However, when the C_v values were 314% and 1000%, the compressive residual stress values saturated at $G = 16$ GW/cm². The amount of heat input increases as the value of G increases. Therefore, it was expected that the compressive residual stress would become small. When the C_v was 314%, the compressive residual stress values were smaller than those at other C_v values.

When SP was applied to Si₃N₄/SiC, the compressive residual stress on the surface was about 1500 MPa and the introduction depth was about 40 μm , as

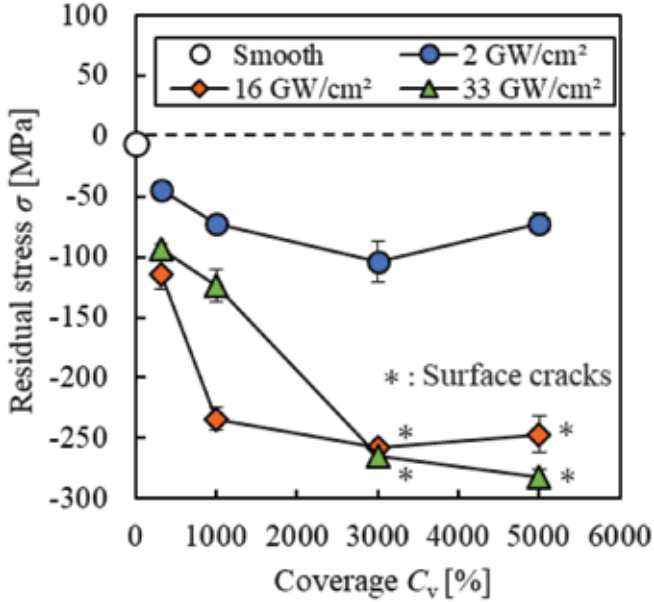


FIGURE 4
Surface residual stress at each power density and coverage.

shown in Figure 6. The residual stress of the shot-peened specimen greatly decreased and approached 0 MPa as the depth exceeded 20 μm . On the other hand, the laser-peened specimen retained the compressive residual stress even at a depth of 40 μm . From this observation, it was concluded that although the laser-peened sample had a smaller surface residual stress than the shot-peened sample, the compressive residual stress could be introduced deeper below the surface. The optimal LP conditions were found to be a G value of 16 GW/cm^2 and a C_v of 1000%. This is because the surface compressive residual stress was the largest among the specimens with no surface cracking after LP.

4 CONCLUSIONS

LPwC was applied to $\text{Si}_3\text{N}_4/\text{SiC}$ composite materials to increase the surface strengths of the ceramics. The influences of LP on the surface conditions, surface roughness, and distribution of residual stress in the depth direction were investigated.

- (1) Surface roughness increased by LP due to laser ablation. When the LP parameters such as power density and coverage were too high, surface cracks appeared on the sample.

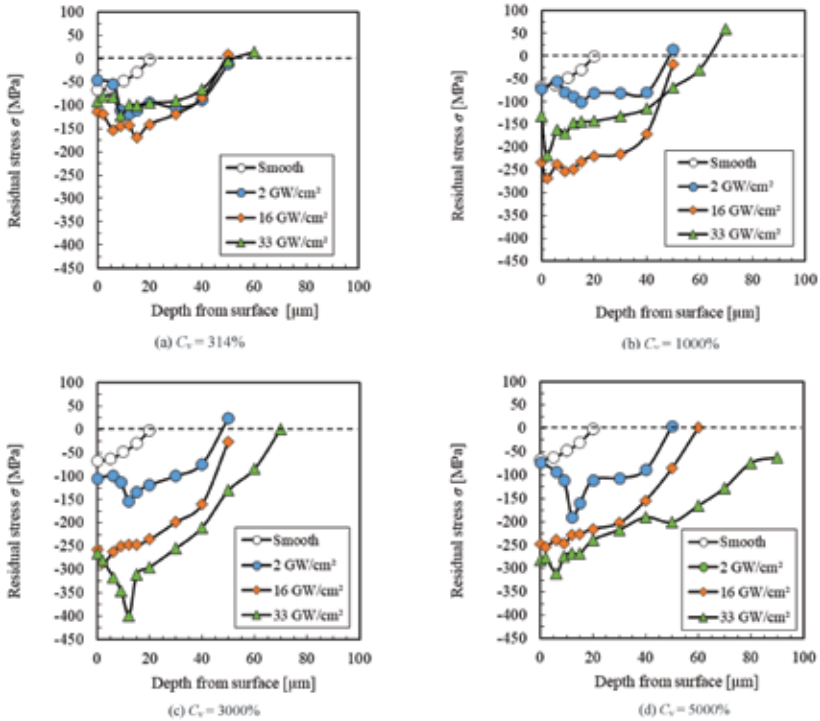


FIGURE 5 Residual stress distributions for $\text{Si}_3\text{N}_4/\text{SiC}$ samples after LP.

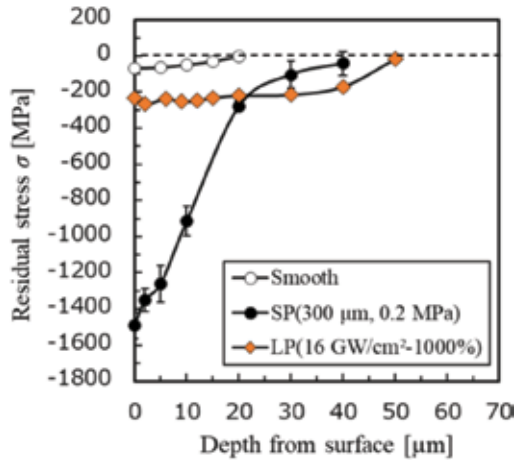


FIGURE 6 Comparison of residual stress distributions of laser-peened and shot-peened specimens.

- (2) Compressive residual stresses up to 230 MPa were introduced by LP without peeling or chipping of the surface.
- (3) The depth of the compressive residual stress was about 50 μm . The surface compressive residual stress of the laser-peened specimen was smaller than that of the shot-peened specimens. However, the depths of compressive residual stress in laser-peened specimens were deeper than those of the shot-peened specimens.

Nomenclature

- t Pulse duration (ns)
 D Spot diameter of the laser (mm)
 E_p Pulse energy (mJ)
 N_p Irradiation density (mm^{-2})
 G Power density (GW/cm^2)
 A_p Spot area (mm^2)
 C_v Coverage (%)
 R_a Arithmetic average surface roughness (μm)

Greek symbols

- λ Wavelength of pulse laser (nm)
 σ Residual stress (MPa)

ACKNOWLEDGMENT

The study was supported in part by a grant for Scientific Research (B) (16H04231) from the Ministry of Education, Culture, Sports, Science, and Technology of Japan.

REFERENCES

- [1] Itoh Y., Suyama S. and Fuse T. Effect of soft shot peening on bending strength of partially stabilized zirconia. *Journal of the Ceramic Society of Japan* **111** (2003), 776–780.
- [2] Moon W., Ito T., Uchimura S. and Saka H. Toughening of ceramics by dislocation sub-boundaries. *Materials Science and Engineering A* **387** (2004), 837–839.
- [3] Tanaka K., Akiniwa Y. and Morishita Y. Residual stress distribution in the sub-surface region of shot-peened ceramics. *Transactions of the Japan Society of Mechanical Engineers Part A* **71** (2005), 1714–1721.
- [4] Pfeiffer W. and Frey T. Strengthening of ceramics by shot peening. *Journal of the European Ceramic Society* **26** (2006), 2639–2645.
- [5] Takahashi K., Nishio Y., Kimura Y. and Ando K. Improvement of strength and reliability of ceramics by shot peening and crack healing. *Journal of the European Ceramic Society* **30** (2010), 3047–3052.
- [6] Koike H., Iwanaka K. and Takahashi K. Measurement of sliding wear of shot-peened Partially Stabilized Zirconia plate. *Applied Mechanics and Materials* **597** (2014), 353–357.

- [7] Takahashi K., Iwanaka K., Osada T. and Koike H. Increase in strength of partially stabilized zirconia after shot peening. *Journal of Materials Engineering and Performance* **24** (2015), 3573–3578.
- [8] Shukla P. and Lawrence J. Micro-shot peening of zirconia-advanced ceramic: an examination of surface integrity. *Journal of Material Science* **50** (2015), 1728–1739.
- [9] Montross C., Wei T., Ye L., Clark G. and Mai Y. Laser shock processing and its effects on microstructure and properties of metal alloys: A review. *International Journal of Fatigue* **24** (2002), 1021–1036.
- [10] Sano Y., Mukai N., Okazaki K. and Obata M. Residual stress improvement in metal surface by underwater laser irradiation. *Nuclear Instruments and Methods in Physics Research B* **121** (1997), 432–436.
- [11] Sano Y., Obata M., Kubo T., Mukai N., Yoda M., Masaki K. and Ochi Y. Retardation of crack initiation and growth in austenitic stainless steels by laser peening without protective coating. *Material Science and Engineering A* **417** (2006), 334–340.
- [12] Zhang X., Zhang Y., Lu J., Xuan F., Wang Z. and Tu S. Improvement of fatigue life of Ti-6Al-4V alloy by laser shock peening. *Material Science and Engineering A* **527** (2010), 3411–3415.
- [13] Hatamleh O., Lyons J. and Forman R. Laser and shot peening effects on fatigue crack growth in friction stir welded 7075-T7351 aluminum alloy joints. *International Journal of Fatigue* **29** (2007), 421–434.
- [14] Wang J., Zhang Y., Chen J., Zhou J., Ge M., Lu Y. and Li X. Effects of laser shock peening on stress corrosion behavior of 7075 aluminum alloy laser welded joints. *Material Science and Engineering A* **647** (2015), 7–14.
- [15] Li Y., Zhou L., He W., He G., Wang X., Nie X., Wang B., Luo S. and Li Y. The strengthening mechanism of a nickel-based alloy after laser shock processing at high temperatures. *Science and Technology of Advanced Materials* **14** (2013), 055010.
- [16] Akita K., Sano Y., Takahashi K., Tanaka H. and Ohya S. Strengthening of Si₃N₄ ceramics by laser peening. *Material Science Forum* **524** (2006), 141–146.
- [17] Shukla P., Smith G., Waugh D. and Lawrence J. Development in laser peening of advanced ceramics. *International Society for Optics and Photonics* **9657** (2015), 77–85.
- [18] Shukla P., Nath S., Wang G., Shen X. and Lawrence J. Surface property modifications of silicon carbide ceramic following laser shock peening. *Journal of the European Ceramic Society* **37** (2017), 3027–3038.
- [19] Shukla P., Robertson S., Wu H., Telang A., Kattoura M., Nath S., Mannava S., Vasudevan V. and Lawrence J. Surface engineering alumina armour ceramics with laser shock peening. *Materials and Design* **134** (2017) 523–538.
- [20] Shukla P. and Lawrence J. Laser shock peening of Si₃N₄ ceramics: Experimental set-up and general effects. *Science and Technology Facilities council* **40** (2014/15).
- [21] Shukla P. and Lawrence J. Alteration of fracture toughness (K_{Ic}) of Si₃N₄ advanced ceramics by laser shock peening. *Science and Technology Facilities council* **41** (2014/15).
- [22] Shukla P. Laser shock peening of metals and advanced ceramics. *The Laser User* **87** (2018), 24–25.
- [23] Wang F., Zhang C., Lu Y., Nastasi M. and Cui B. Laser shock processing of polycrystalline alumina ceramics. *Journal of the American Ceramic Society* **100** (2017), 911–919.
- [24] Wang F., Zhang C., Yan X., Deng L., Lu Y., Nastasi M. and Cui B. Microstructure-property relation in alumina ceramics during post-annealing process after laser shock processing. *Journal of the American Ceramic Society* **101** (2018), 4933–4941.
- [25] Xing Y., Deng, J., Zhang, K., Zhang G. and Gao H. Effect of femtosecond laser pretreatment on wear resistance of Al₂O₃/TiC ceramic tools in dry cutting. *International Journal of Refractory Metals and Hard Materials* **43** (2014), 291–301.
- [26] Ando K., Takahashi K., Nakayama S. and Saito S. Crack-healing behavior of Si₃N₄/SiC ceramics under cyclic stress and resultant fatigue strength at the healing temperature. *Journal of the American Ceramic Society* **8** (2002), 2268–2272.

Estimation of Laser Shock Peening Induced Plastic Deformation in Hastelloy-X Superalloys

S. NATH*¹, P. SHUKLA¹, X. SHEN¹, A. BEHERA² AND J. LAWRENCE¹

¹*School of Mechanical, Aerospace and Automotive Engineering, Coventry University, Coventry, CV1 2JH, UK*

²*Department of Metallurgical and Materials Engineering, National Institute of Technology, Rourkela, 769008, India*

The goals of the present study are to strengthen a new, Hastelloy-X superalloys by prestressing the surface with laser-plasma driven shock waves and also to quantify the effect of Laser Shock Peening (LSP) on the evolution of phase, residual stress (both through thickness and on the surface), dislocation density, and hardness of Hastelloy-X superalloys. Dislocation densities in the peened and unpeened samples were measured by Williamson and Smallman approach to analyze the severity of plastic deformation following LSP surface treatment. The maximum compressive residual stress measured on the peened surface of Hastelloy-X samples using incremental hole drilling technique was 850 MPa. In addition, it was found that the LSP parameters have a dominant effect in tailoring the surface hardening behavior and residual stress in Hastelloy-X superalloys.

Keywords: Laser shock peening, residual stress, incremental hole drilling, dislocation density, strain hardening

1 INTRODUCTION

Hastelloy-X is a solid solution-strengthened nickel-based superalloy with excellent oxidation resistance, formability, and high-temperature strength [1-3]. Hastelloy-X superalloys are extensively used in gas turbine engines for combustion-zone components, tail pipes, and are being considered as potential material for high-temperature gas-cooled reactor (HTGR) [4]. However, failure in these materials was reported due to intergranular attack and internal

Corresponding author's e-mail: sendsubha@gmail.com

oxidation in high-temperature gas mixtures [3, 5]. The thermal stress induced cracks are responsible for the generation of intergranular attacks and occurrence of internal oxidation in Hastelloy-X superalloys.

Laser shock peening (LSP) is a surface severe plastic deformation process which involves plastic deformation of the material by high pressure shock waves resulting from interaction of energetic laser with a material [6, 7]. The generated shock waves not only deform the material in contact plastically, but also induce compressive residual stress on the surface of the material [7-10]. The generation of compressive residual stress helps to delay the crack growth/propagation, thereby increasing the fatigue strength of the material [11, 12]. The use of LSP process has also been extended to strain harden materials' surface which increases the hardness, toughness and tribological properties of the metallic and ceramic systems [10, 13, 14].

LSP of many advanced materials have been investigated which include aluminum alloys [15- 19], nickel alloys [20-29], titanium alloys [30- 35], iron alloys [36-40], magnesium alloys [41, 42], copper alloys [43] etc. Interestingly, LSP studies have not been limited to only metallic systems, it has also been studied on non-metallic systems [13, 14]. The LSP of these conventional and advanced materials have shown to improve not only the surface hardening and fatigue strength, but also significantly contributed to the improvement of corrosion and wear resistance properties [30, 44]. Grain size reduction and surface nano-crystallizations have also been observed following LSP [19, 42]. The work carried out by Tradan *et al* [19] showed an increase in the dislocation density following LSP which was responsible for the evolution of ultra-fine grains in the near surface microstructure.

Studies on LSP of Ni-based superalloys were mostly reported on the mechanical properties and residual stress development. Gill *et al* [26] compared the effect of advanced mechanical surface treatments (laser shock peening, cavitation shotless peening and ultrasonic nanostructure modification) on IN718 SPF and investigated the process effect on residual stress development, surface hardening, microstructural evolution etc. The measured residual stress and hardness were lowest amongst all the three surface treatment processes with no signature of nano-crystallization [26]. Wang *et al* [20], however, reported grain refinement following LSP of K403 Ni alloy. The studies on LSP of Ni-based superalloys depict only on qualitative dislocation density without providing the much needed quantitative information.

The aim of the present investigation is to study the effect of LSP on the properties of Hastelloy-X superalloys and to understand the strengthening mechanisms. The study is mainly focused on studying the phase distribution/evolution, microstrain development, surface hardening behavior, and evolution of dislocation density and residual stress following LSP. Microstrain and dislocation density have been measured and critically discussed to understand the strain hardening behavior in Hastelloy-X superalloys following LSP. In-depth residual stress measurement has been carried out using incre-

TABLE 1

Nominal composition and mechanical properties of Hastelloy-X used for LSP.

Composition (wt.%)							Young's modulus (GPa)	Yield strength (MPa)	Dynamic yield strength (MPa)
Ni	Cr	Fe	C	Mo	Si	W			
Bal.	20	19.8	0.1	7	0.3	0.5	190	380	570[45]

mental hole drilling technique to quantify the depth of residual stress in the material following LSP surface treatment.

2 MATERIALS AND METHODS

2.1 Materials

LSP was carried out on rectangular Hastelloy-X superalloy samples (30 mm × 10 mm × 10 mm dimension), whose composition and mechanical properties are mentioned in Table 1. Prior to LSP, these superalloy samples were stress relieved at 1175 °C for an hour followed by grinding in 600 µm grit size SiC papers to remove the surface residues and oxides. Ultrasonic cleaning was carried out in acetone and isopropyl alcohol baths to remove any contaminants present on the surface followed by blower drying.

2.2 Laser shock peening

In the present study, a 10 J pulsed Nd:YAG laser system (LPY10J; Litron) was used for the laser shock peening (LSP) study. The schematic of the LSP set up is shown in Fig.1. The LSP studies were carried out with a radiation wavelength of 1064 nm and a pulse duration of 8 ns long at a repetition rate of 10 Hz. The raw beam diameter was 25 mm which was then focused down to 3 - 7.5 mm on the sample's surface using a fused silica lens (focal length = 50 mm). The laser beam divergence was 0.5 mrad ($M^2 \approx 1.99$). The laser beam radiance density were measured to be between 6.44 to 22.65 J.cm².Sr⁻¹.µm [46–49]. Black polyisobutylene tape with a thickness of 500 µm was used as an absorptive layer to prevent any thermal effect on the sample during LSP process. Water with a flow rate of 2 L/min was used as a confinement medium in the present study. All the samples were treated with single shot laser pulse with an overlap of 50%. The process map adopted in the present study are presented in Figure. 2. Four different systems were developed based on the laser energy and beam diameter combinations. This led to four different laser power densities used in the present study.

LSP involves irradiating the surface of the target using a high energy laser which then forms an expanding plasma, following laser-material interaction, with high pressure shock waves propagating into the material. The material is

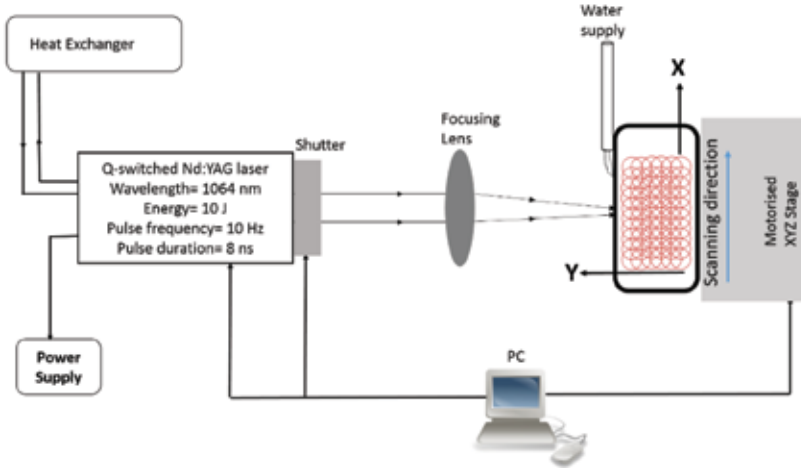


FIGURE 1
Schematic representation of laser shock peening (LSP) process.

considered to deform plastically when the shock wave pressure exceeds the Hugoniot Elastic Limit (*HEL*) of the material.

According to Fabbro *et al* [50] and Peyre *et al* [7, 8], the peak plasma pressure, P , can be expressed as

$$P(GPa) = 0.01 \sqrt{\frac{\alpha}{2\alpha + 3}} \sqrt{Z \left(\frac{g}{cm^2 s^2} \right)} \sqrt{I_0 \left(\frac{GW}{cm^2} \right)} \quad (1)$$

where, $I_0 \left(= \frac{P_{avg}}{f \times \tau \times A} \right)$ is the laser power density and P_{avg} , f , τ , A , Z , and α are the average power (W), pulse repetition rate (Hz), pulse duration (ns), laser spot area (cm^2), reduced shock impedance between the material and the confining medium, and efficiency of plasma-material interaction (0.1 – 0.2) [8], respectively. The importance of α during laser-material interaction is that it contributes to the total energy (E_t) by converting part of energy (αE) to thermal energy and rest of the energy ($(1 - \alpha)E$) is used to generate and ionize plasma. The increased in thermal energy increases the pressure of the plasma.

The reduced shock impedance is expressed as [8]

$$\frac{2}{z} = \frac{1}{z_1} + \frac{1}{z_2} \quad (2)$$

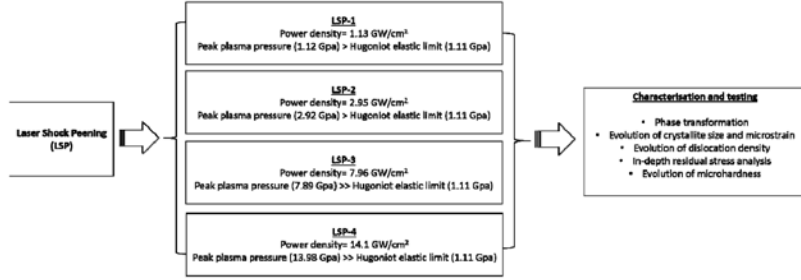


FIGURE 2
Process Map For The Laser Shock Peening Of Hastelloy-X Superalloys.

where, Z_1 and Z_2 are the shock impedances of target material and confining medium, respectively. In the present study, Z_1 (nickel) = $4.14 \times 10^6 \text{ g cm}^{-2} \text{ s}^{-1}$ and Z_2 (water) = $0.165 \times 10^6 \text{ g cm}^{-2} \text{ s}^{-1}$ [20].

The reduced shock impedance according to Equation. (2) is measured to be $0.32 \times 10^6 \text{ g cm}^{-2} \text{ s}^{-1}$. The value of peak pressure developed on the sample's surface following LSP was calculated according to Equation. (1) is shown in Figure. 2. The *HEL* of any material is related to its dynamic yield strength ($\sigma_{Y,dyn}$) as [6, 45]

$$HEL = \frac{1 - \nu}{1 - 2\nu} \sigma_Y^{dyn} \quad (3)$$

where, ν is the Poisson's ratio of the material. The value of σ_Y^{dyn} was taken from ref. [45] for the calculation of *HEL*. The calculated value of *HEL* was measured using Equation. (3) and is shown in Figure. 2.

The laser shock peening parameters were chosen to ensure that the peak plasma pressure exceeds the *HEL* of the material to plastically deform the material.

2.3 Material characterization

2.3.1 Phase analysis

X-ray diffraction (XRD) (D8 Discover; Bruker Corporation) was used to study the phase evolution following LSP using a Cu $K\alpha$ radiation with a scan step of $0.02^\circ/\text{s}$ and time per step of 0.1 s. For the measurement of full width at half maximum (FWHM) of the diffraction peaks, scanning speed of $0.01^\circ/\text{s}$ and time per step of 5 s were employed to ensure higher peak counts. Each peak was then fitted using Pseudo-Voigt function with Origin8.5 software platform.

The Williamson-Hall method for Uniform Stress Deformation Model (USDM) considering the anisotropic nature of the strain was used for the determination of microstrain developed in the crystal lattice following LSP. The equation used to calculate the microstrain is presented below [51, 52].

$$\beta_{hkl} \cos \theta_{hkl} = \frac{k\lambda}{D} + 4 \left(\frac{\sigma}{E_{hkl}} \right) \sin \theta_{hkl} \quad (4)$$

where, β is the full width half maximum (FWHM), θ is the diffraction angle, K (≈ 1) is a constant, λ is the X-ray wavelength, and D is the crystallite size (or domain size). The suffix, hkl , refers to a crystallographic plane.

From the slope and intercept of the plot between $\beta_{hkl} \cos \theta$ and $4 \sin \theta / E_{hkl}$, the lattice deformation stress, σ , and the crystallite size, D , were measured, respectively.

The microstrain (ϵ) can be re-written as $\left(\epsilon^{hkl} = \frac{\sigma}{E_{hkl}} \right)$, where E_{hkl} is the Young's modulus in a crystallographic direction perpendicular to the lattice plain (hkl).

2.3.2 Microstructural analysis

Optical microscopy of the LSP treated surface was carried out using a light optical microscope (Axio Observer; ZIESS) to measure the grain size. The grain size was measured using linear intercept method according to ASTM E112 – 13. Microstructural analysis of the LSP treated surface was carried out using scanning electron microscope (SEM) (Gemini SEM; ZIESS). The samples were chemical etched prior to microstructural study. The etchant used to etch Hastelloy-X samples was Waterless Kalings reagent. The etching time was optimized to be 30 seconds for Hastelloy-X samples.

2.3.3 Dislocation density measurement

Williamson and Smallman method [53] was used to measure dislocation density in untreated and LSP treated samples. The method assumes the crystallite size and microstrain are related to dislocation density as:

$$\rho = \frac{2\sqrt{3} \langle \epsilon^2 \rangle^{1/2}}{Db} \quad (5)$$

where, $\langle \epsilon^2 \rangle^{1/2}$ is the root mean square (rms) microstrain, D is the size of coherently diffracting domains, and b is the burger vector in $\langle 110 \rangle$ direction and for an FCC crystal it is expressed as $b = \langle 110 \rangle a/2$, where a is the lattice

parameter. The lattice parameter was measured using XRD and it was to be 0.355 nm for Hastelloy-X superalloy.

2.3.4 Residual stress measurement using incremental hole drilling technique

The incremental hole drilling technique was used to measure residual stress along the depth of the sample. The measurement was carried out using a hole drilling apparatus (Restan-MTS3000; SINT Technologies) which consists of both the mechanical and electronic drills. For this study here, the electrical drill was employed. The obtained data was then evaluated by a control software (RMS) and back calculation software (EVAL). The drilling device was mounted using magnetic feet on a 12 mm thick mild steel plate. The identification of the surface of the sample (reference point for drilling) was controlled by the electrical contact between the endmill and the metallic sample. The end mill diameter was 1.5 mm. The drilling speed was kept at 0.1 mm/min. The acquisition delay and the drilling delay were kept at 4s and 3s, respectively. The residual stresses were calculated by the HDM method using the constant spline function with eccentricity correction between the drilled hole and the center of the strain gage rosette.

2.3.5 Microhardness Measurement

Vickers microhardness tester (DURASCAN-70; Struers) was used to measure the hardness of untreated and LSP treated samples using 100 gf load and a dwelling time of 10 seconds.

3. RESULTS

3.1 Microstructural characterisation

Figure. 3 shows the optical micrographs of (a) LSP-1, (b) LSP-2, (c) LSP-3, (d) LSP-4, and (e) unpeened sample. Surface microstructure modification is evident from the cross-section of optical micrographs following LSP. The depth of microstructural modification varies between 40 to 90 μm as shown by the dotted lines. Higher depth of microstructural modification can be observed for sample treated with a peak power density of 14.1 GW/cm^2 (LSP-4). The grain sizes were measured on three different samples using linear intercept method (ASTM E112 – 13) and the lowest grain size of 23 μm ($\pm 1.5 \mu\text{m}$) was measured for LSP-4 (14.1 GW/cm^2). The measured grain size for LSP-1 (1.12 GW/cm^2), LSP-2 (2.95 GW/cm^2), and LSP-3 (7.96 GW/cm^2) were 30 μm ($\pm 2.8 \mu\text{m}$), 28 μm ($\pm 2.3 \mu\text{m}$), and 25 μm ($\pm 1.8 \mu\text{m}$), respectively. The measured grain size in an unpeened sample was 57 μm ($\pm 5.2 \mu\text{m}$).

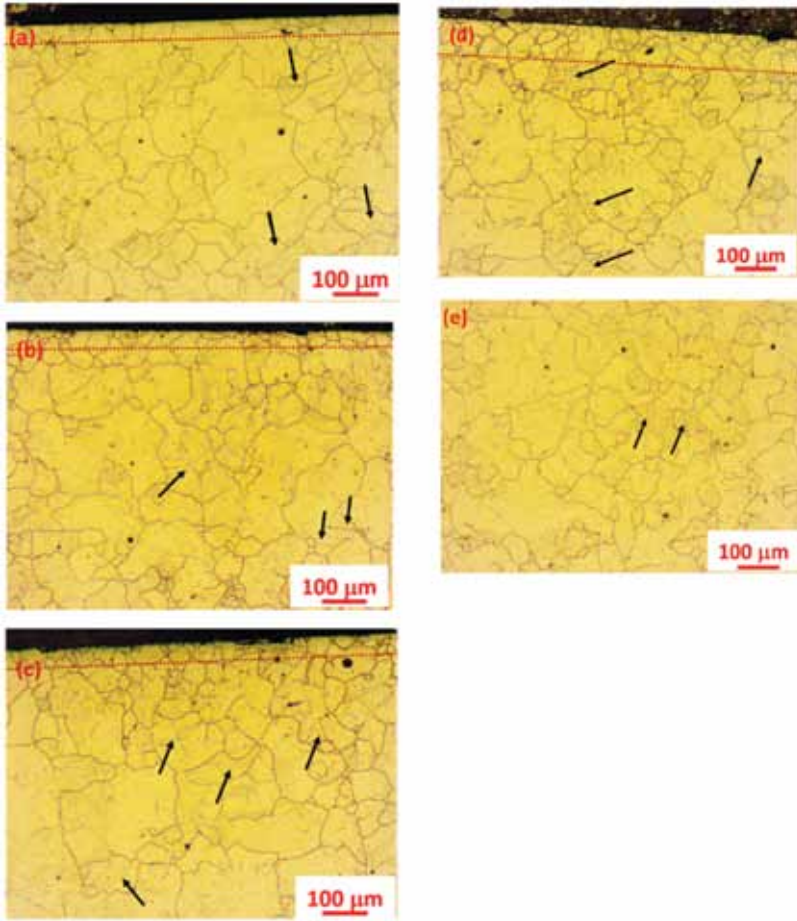


FIGURE 3

Cross-sectional optical micrographs of (a) LSP-1, (b) LSP-2, (c) LSP-3, (d) LSP-4, and (e) unpeened sample.

Figure. 4 shows the scanning electron micrograph of the cross-section of (a) LSP-1, (b) LSP-2, (c) LSP-3, and (d) LSP-4. From Figure. 4 (a-d), the deformation induced grain size reduction is evident. Hastelloy-X is a solid solution strengthened Ni-Fe superalloy. Presence several annealing twins in the austenitic matrix is evident in the microstructure of the Hastelloy-X superalloys which formed due to solution annealing treatment of samples to relieve any trapped stress before LSP.

High magnification scanning electron micrographs of an unpeened sample (Figure. 5a) and LSP-4 (Figure. 5b) are shown in Figure. 5. The high magnification micrographs don't show any sign of significant microstructural refinement with only presence of sub-grains (as shown by arrows) in a grain

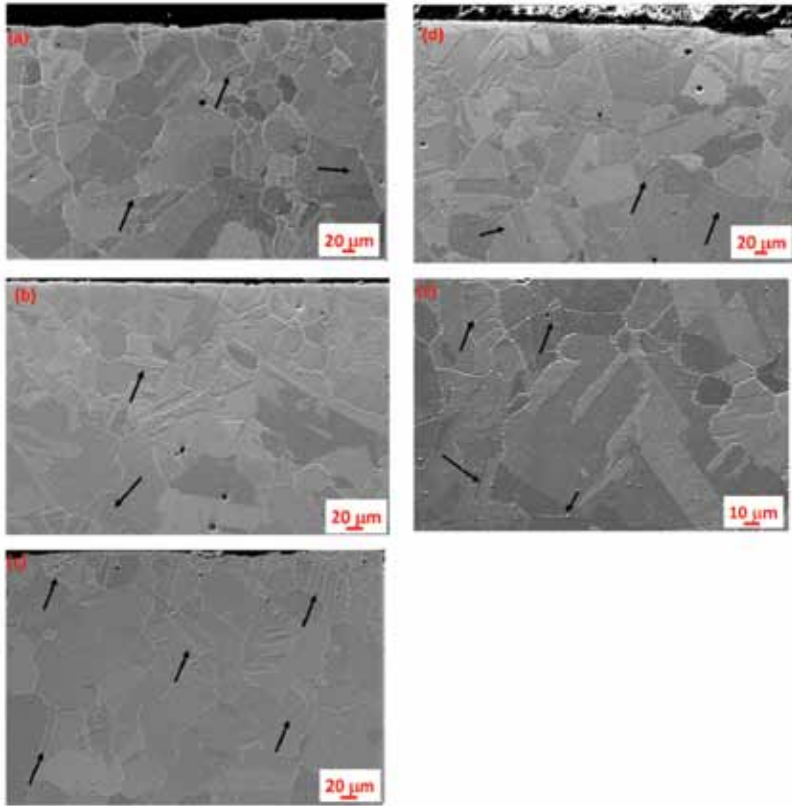


FIGURE 4
Cross-sectional scanning electron micrographs of (a) LSP-1, (b) LSP-2, (c) LSP-3, (d) LSP-4, (e) unpeened sample.

as shown in Figure. 5b with the dotted line. No evidence of surface melting is also observed in Figure. 5b which confirms the process was purely mechanical without any thermal effect.

3.2 Phase analysis

Figure. 6 shows the XRD phase scans of an untreated Hastelloy-X superalloy (plot 1), LSP-1 (plot 2), LSP-2 (plot 3), LSP-3 (plot 3), and LSP-4 (plot 5). The XRD phase scans reveal presence of face centered cubic (FCC) reflections of nickel (Ni) matrix in both untreated and laser shock peened samples. There is no trace of reflections from any other phase suggesting that there was no separate phase formation (oxides) or phase transformation due to high pressure shock waves during LSP which corroborates microstructural studies indicating absence of melting (no thermal effect). The lattice parameter in the unpeened and LSP treated Hastelloy-X samples were measured to be 0.355

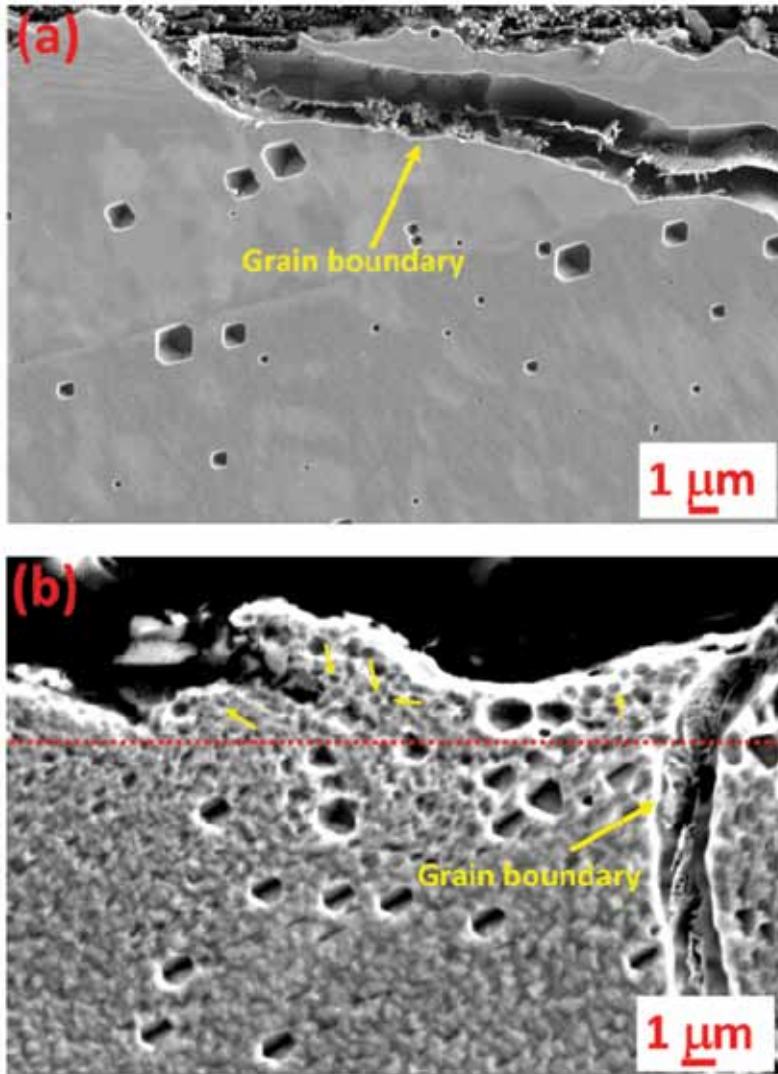


FIGURE 5 Scanning electron micrographs of cross-section of (a) as-received Hastelloy-X and (b) LSP-4.

nm which was used to calculate burger vector in the $\langle 110 \rangle$ direction and hence, the dislocation density.

The crystallite size (D) and *rms* microstrain (ϵ_{rms}) in laser shock peened samples were estimated from the XRD peak broadening using Uniform Stress Deformation Model (USDM) and the estimated values are plotted in Figure. 7. It should be noted here that, D is the size of the homogeneous domains contributing to coherent diffraction under XRD, and is less than the grain

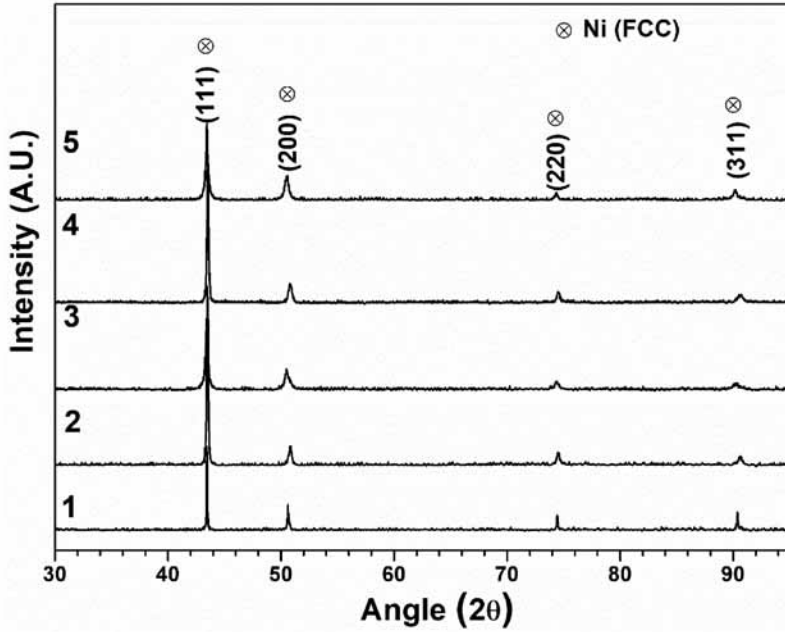


FIGURE 6 X-ray diffraction scans of an untreated hastelloy x superalloy (plot 1), LSP-1 (plot 2), LSP-2 (plot 3), LSP-3 (plot 3), and LSP-4 (plot 5).

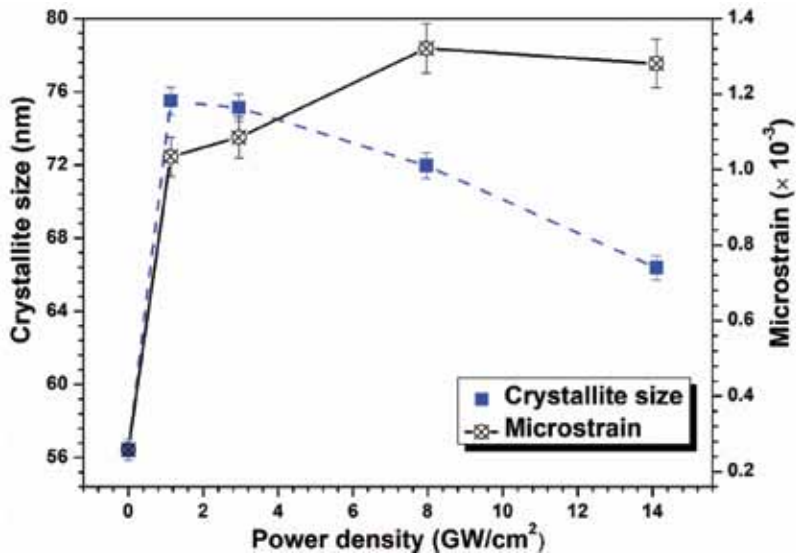


FIGURE 7 Variation of crystallite size and microstrain with laser power density.

size, which was estimated by optical microscopy and scanning electron microscopy. On the other hand, dislocations are considered to be the line defects which are responsible for the peak shift, broadening and asymmetry in the XRD pattern. The measurement and analysis of dislocation density and peak broadening are discussed in the following sections. The crystallite size of an untreated Hastelloy-X superalloy was measured to be 56 nm. It is interesting to note that with the application of LSP surface treatment the crystallite size increases which is evident from Figure. 7. The crystallite sizes of LSP-1, LSP-2, LSP-3, and LSP-4 were measured to be 76 nm, 75 nm, 72 nm, and 66 nm, respectively. From Figure. 7, it can be observed that the crystallite size decreases with increase in the laser power density which implies that higher the plastic deformation, the lower is the crystallite size. The root mean square (*rms*) microstrains were measured using the microstrains observed in different crystallographic directions. Figure. 7 shows the *rms* microstrain developed on the laser shock peened samples. The microstrain measured in the Hastelloy-X samples were also found to be dependent on the laser power density. With the increase in the laser power density, the microstrain developed on the surface of the sample increases as shown in Figure. 7.

Figure. 8 shows the variation of dislocation density with laser power density. Measuring dislocation density in laser shock peened samples is an effective way to quantify plastic deformation. High strain rate surface plastic deformation of the metallic systems were reported to increase the dislocation

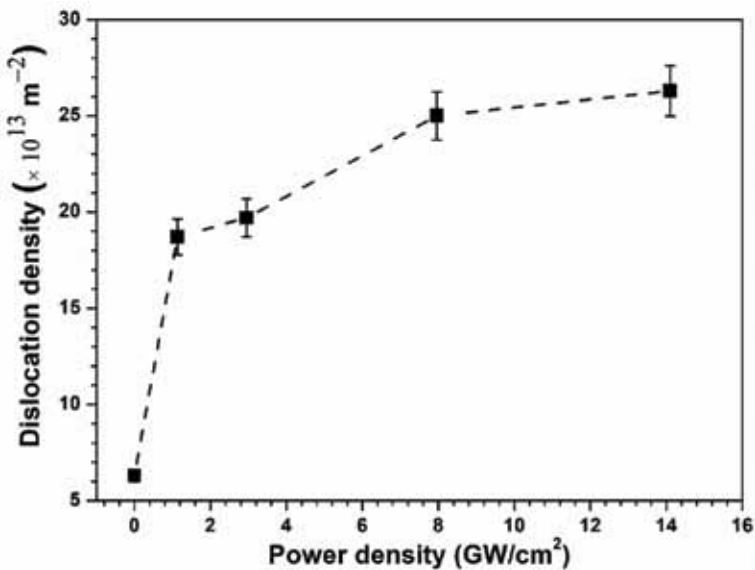


FIGURE 8
Variation of dislocation density with laser power density.

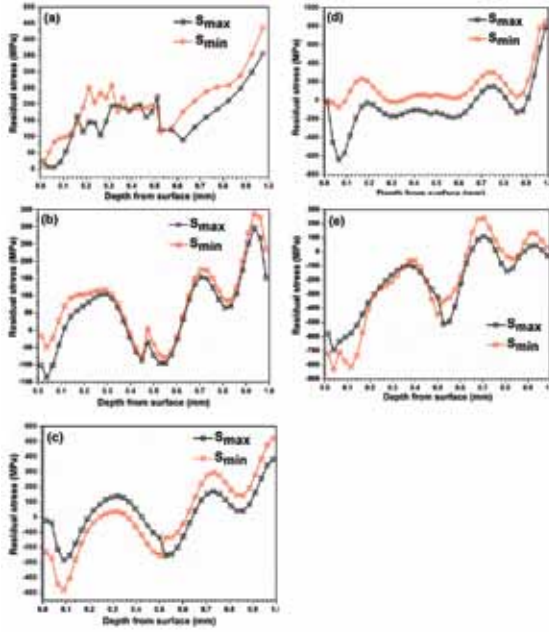


FIGURE 9
Incremental hole drilling residual stress measurement of (a) as-received Hastelloy-X sample, (b) LSP-1, (c) LSP-2, (d) LSP-3, and (e) LSP-4.

density which resulted in surface hardening as well as formation of nano-structured zone on the surface [24, 54]. From Figure. 8, it may be noted that the dislocation density in an untreated sample is $6.3 \times 10^{13} \text{ m}^{-2}$ which increases to a maximum value of $26.3 \times 10^{13} \text{ m}^{-2}$ for LSP-4. The dislocation density in LSP-1, LSP-2, and LSP-3 were measured to be $18.7 \times 10^{13} \text{ m}^{-2}$, $19.7 \times 10^{13} \text{ m}^{-2}$, and $25 \times 10^{13} \text{ m}^{-2}$, respectively.

3.3 Incremental hole drilling

LSP is a process where plastic loading and unloading takes place which leads to the development of compressive residual stress in the material. Residual stress distributions in the untreated and LSP treated samples as a function of depth are shown in Figure. 9 (a-e). Stresses were measured in two directions perpendicular to each other. The initial stress on the untreated sample's surface is tensile in nature ($S_{\text{max}} = 23 \text{ MPa}$ and $S_{\text{min}} = 9 \text{ MPa}$) as shown in Figure. 9 (a). From Figure. 9 (b-e), it can be observed that the LSP treated samples shows development of compressive residual stress following LSP and the maximum compressive residual stress was measured just below the surface. The compressive nature of the residual stress developed on the samples following LSP confirms the theoretical

data shown in Figure. 2. It is to be noted that the depth of compressive residual stresses in LSP-1 to LSP-4 varies between 0.1 mm to 0.35 mm. The previous studies have shown the depth of compressive stress is extended up to 1 mm [24, 54, 55]. The difference in depth of compressively stressed zone in the present study and previous studies may be attributed to the use single shot laser pulse instead of multiple shots [55]. This is because of the work hardening of the material due to dislocations generation in first shot which then decreases the rate of attenuation of the subsequent pressure pulse followed by a higher peak pressure to deform deeper into the material on successive shots. The compressive residual stress components S_{\max} and S_{\min} for LSP-1 were measured to be 140 MPa and 50 MPa, respectively as shown in Figure. 9 (b). Residual compressive stress components for LSP-2 were 481 MPa (S_{\max}) and 280 MPa (S_{\min}) as shown in Figure. 9 (c). Maximum compressive residual stresses of 697 MPa (S_{\max}) and 834 MPa (S_{\min}) were measured at 39 mm below the surface for LSP-3 as shown in Figure. 9 (d). On the other hand, the compressive residual stresses measured for LSP-4 were 637 MPa (S_{\max}) and 73 MPa (S_{\min}).

4 DISCUSSION

LSP is a high strain rate deformation process which results in producing nanostructured zones in the surface microstructure. Table 2 compares the results obtained in the present study and reported works on LSP of Ni-based superalloys. These will be discussed in the following section. It is important to mention here that no other studies on LSP of Ni-based alloys have used incremental hole drilling technique to measure the residual stress through depth.

Following grain size measurements using Figure. 3 (a-d), a maximum reduction in grain size of 60% with a laser power density of 14.1 GW/cm² was observed. The increased shock wave pressure at higher laser power density is the reason behind the reduction in grain size. Hua *et al* [25] reported similar reduction in grain size following LSP. The reported value of grain size following LSP was 18.5 nm as compared to 33.3 nm in an untreated GH586 superalloy. The grain size reduction observed in the present study is not so significant as compared to several other studies where grain sizes were in the order of nanometer following LSP [24, 54]. However, reported studies were conducted with multiple laser shots during LSP which resulted in a grain size reduction whereas a single-shot strategy was used in the present study. Studies carried out by Trdan *et al* [19] and Kattoura *et al* [24] showed the grain size in the near surface regions were in the range of 20-50 nm following LSP Al-Mg-Si alloys and ATI 718Plus alloy, respectively. Interestingly, a laser power density of 4.7 GW/cm² was shown to produce a nanostructured zone

TABLE 2
Reported works on LSP of Ni-based alloys and its comparison with the present study.

Ni-based alloy	Laser energy (J)	Laser intensity (GW/cm ²)	Residual stress (MPa)	Hardness	Ref.
Hastelloy-X superalloy	Wavelength = 1064 nm; Pulse energy= 8 J; Pulse duration= 8 ns; Pulse repetition rate= 10 Hz; Spot diameter= 3-7.5 mm; Overlap= 50%	1.13 - 14.1	Untreated= 23 (S _{max}) ^e and 9 (S _{min}) ^e ; LSP= 697 (S _{max}) ^e and 834 (S _{min}) ^e	Untreated= 208 HV0.1 ^a , LSP= 243 HV0.1 ^a (1 shot)	Present study
K403 nickel alloy	Wavelength = 1064 nm; Pulse energy= 5-25 J; Pulse duration= 20 ns; Pulse repetition rate= 1 Hz; Spot diameter= 2 mm; Overlap= 60%	12	LSP= -633 (1 shot) ^d ; -826 (2 shot) ^d ; -882 (3 shot) ^d	Untreated= 389 HV0.3 ^a ; LSP= 453 HV0.3 ^a (1 shot); 461 HV0.3 ^a (2 shot); 475 HV0.3 ^a (3 shot)	[20]
Inconel alloy 718	Wavelength = 1054 nm; Pulse energy= 1.5-3.9 J; Pulse duration= 20 ns; Spot diameter= 1.8 mm; Overlap= 50%	2.9 - 7.7	LSP= -550 ^d		[21]

Single crystal Ni-superalloy	Wavelength = 1064 nm; Pulse energy= 6 J; Pulse duration= 14 ns; Pulse repetition rate= 2 Hz; Spot diameter= 2 mm; Overlap= 0%	13.6	~7.1 GPa ^{ab} (~724 HV)	[22]
Incoloy 800 superalloy	Wavelength = 1064 nm; Pulse energy= 0.4 J; Pulse duration= 10 ns; Pulse repetition rate= 10 Hz; Spot diameter= 3 - 6 mm		LSP= -227 ^d	[23]
ATI 718 Plus superalloy	Wavelength = 1064 nm; Pulse energy= 3 J; Pulse duration= 20 ns; Pulse repetition rate= 10 Hz; Spot diameter= 2 mm; Overlap= 50%	4.7	Untreated= -160 (X) ^d and -69 (Y) ^d LSP= -746 (X) ^d and -695 (Y) ^d	[24]
GH586 superalloy	Wavelength = 1064 nm; Pulse energy= 15 J; Pulse duration= 30 ns; Spot diameter= 4 mm; Overlap= 50%		Untreated= 6.71 GPa ^{ab} (~684 HV); LSP= 8.33 GPa ^{ab} (~849 HV) LSP= ~510.3 HV0.2 ^a	[25]
Inconel 718 SPF superalloy	Wavelength = 1054 nm; Pulse energy= 8.23 and 15.24 J; Pulse duration= 28.6 and 25.3 ns; Spot diameter= 2 and 2.18 mm; Overlap= 50%	9 and 16	LSP= -750 (at 8 J) ^d and -690 (at 16 J) ^d	[26]
Astrolloy superalloy	Wavelength = 1064 nm; Pulse energy= 80 J; Pulse duration= 25 ns; Pulse repetition rate= 1 Hz; Spot diameter= 8 mm	5	LSP= -700 ^d	[27]
K417 superalloy	Wavelength = 1064 nm; Pulse energy= 8 J; Pulse duration= 20 ns; Spot diameter= 3 mm; Overlap= 33 %	11.3	LSP= -600 ^d	[28]
K417 superalloy	Wavelength = 1064 nm; Pulse energy= 10.8 J; Pulse duration= 20 ns; Pulse repetition rate= 1 Hz; Spot diameter= 3.4 mm; Overlap= 60 %	6	Untreated= 380 HV0.2 ^a ; LSP= 445 HV0.2 ^a	[29]

^aVickers Hardness; ^bNano-hardness; ^cKnoop Hardness; ^dX-ray diffraction; ^eHole drilling

near the surface in Ni-based superalloys [24] whereas a laser power density of 14.1 GW/cm^2 in the present study didn't result in the formation of nanometer sized grains in Hastelloy-X samples. No grain refinement in Inconel 718 SPF alloy was, however, observed by Gill *et al* [26] following LSP with a laser power density of 16 GW/cm^2 . The reason of the observation may be related to single-shot LSP strategy. Nonetheless, with the use of single-shot LSP a significant decrease in grain size was observed which would help to fine tune the LSP process further for getting higher surface strength and improved surface properties. A transmission electron microscopy study will be done in future to measure the grain size in the near surface zone. Nonetheless, grain size reduction is evident, however, a nanostructured zone is not evident. Comparing Figure. 5a and Figure. 5b, it may also be noted that the surface of LSP-4 is wavier than the surface of the unpeened sample. The surface waviness is believed to be due to the laser shock wave induced deformation.

In LSP, the severity of plastic deformation increases with the increase in the peak pressure exerted on the sample. The peak plasma pressure can be controlled by exploiting the laser power density and the reduced shock impedance according to Equation. (1). Moreover, the peak plasma pressure can also be controlled by using different absorptive mediums and confining mediums [6, 56, 57]. In the present study, water was used as a confinement medium and black vinyl tape was used as an absorptive medium. However, laser power density was varied.

The increase in dislocation density in the LSP treated samples indicates an increase in the magnitude of plastic deformation which is necessary to obtain a hardened surface and to induce compressive residual stress on the surface of the superalloy. By looking at Equation. (1), it is clear that with the increase in laser power density, the peak plasma pressure on the surface increases. An increased peak plasma pressure then deforms the material by pure mechanical effect. In the present study, a 4-fold increase in the magnitude of dislocation density was observed following LSP with a laser power density of 14.1 GW/cm^2 as shown in Figure. 8. A 2.5 times increase in dislocation density (measured using Smith–Guttman linear intercept technique) was reported by Tradan *et al* [19] following LSP of aluminum alloy. It is to be noted that no reported dislocation density on Ni-based alloys following LSP was found to compare with the present study. The increase in the dislocation density is attributed to the peak plasma pressure of 13.98 GPa (*cf.* Figure. 2) which is much higher than the *HEL* of the material ($\approx 1.11 \text{ GPa}$). Three-fold increase in the dislocation density was also observed when the sample was LSP treated with a laser power density of 1.13 GW/cm^2 as compared to the untreated sample. It is important to mention here that a laser power density of 1.13 GW/cm^2 induces a peak plasma pressure of 1.12 GPa on the surface of the sample as mentioned in Figure. 2. The minimum plasma pressure requires to induce plastic deformation in the

material is 1.11 GPa (\approx HEL). The small difference of $\sim 5\%$ in the measured dislocation density between LSP-1 and LSP-2 is due to the smaller change in the laser power density in LSP-2 than in LSP-1 as shown in Figure. 8. However, a considerable increase in dislocation density of almost 27% can be observed following an increase in the laser power density from 2.95 GW/cm² to 7.96 GW/cm² as evident from Figure. 8 which is attributed to increase in peak plasma pressure. Figure. 8 also depicts that the dislocation density in LSP-4 shows a change of only $\sim 5\%$ as compared to LSP-3. This is almost similar to the difference between LSP-1 and LSP-2. However, the difference in laser power density between LSP-3 and LSP-4 is more as compared to the difference between LSP-1 and LSP-2. It is believed that the confinement layer breakdown phenomenon may be the reason behind the small increase in the dislocation density [6]. Confinement layer breakdown phenomenon indicates that the confining dielectric medium (water in this case) is no more transparent to the incident laser radiation due to increase in plasma in the dielectric volume and the transmission of laser radiation through the confining medium to the interface is severely disrupted by the inverse Bremsstrahlung mechanism. This behavior is characterized by saturation in plasma pressure with increase in laser power density.

The generation of compressive stress is also dependent on the applied laser power density. That is why higher values of compressive stress were measured for LSP-3 and LSP-4 as compared to LSP-1 and LSP-2 samples. It should also be noted that reported results were also shown to have tensile residual stress which is due to surface melting during LSP [21]. The reported compressive residual stress values were between -227 MPa and - 882 MPa [20, 21, 23, 24, 26-29]. The reported compressive residual stresses using single-shot LSP were 633 MPa [20] and 583 MPa [29]. The variation in the reported values and the value measured in the present study is believed to be due to the different LSP conditions/parameters employed herein. Moreover, the LSP-4 sample showed lower stress value than LSP-3 which may be due to the confinement layer break down phenomena. The confinement layer breakdown phenomena is observed when the laser power density increases to a critical value (as happened for LSP-4) beyond which the peak plasma pressure is no longer a linear function of laser power density and a scattered compressive stress may be observed beyond this point [6]. The increased compressive residual stress in Hastelloy-X superalloys following LSP surface treatment may be beneficial in improving the fatigue strength of the superalloy under study which is in scope of future study. The improvement in microhardness is related to the strain hardening phenomena which is observed following LSP surface treatment.

Figure. 10 shows the microhardness distribution in the LSP treated samples LSP-1, LSP-2, LSP-3, and LSP-4. A maximum hardness of 243 HV_{0.1} was measured on the surface of LSP-4. The surface hardness of LSP-1, LSP-2, and LSP-3 were measured to be 212 HV_{0.1}, 223 HV_{0.1}, and 240 HV_{0.1},

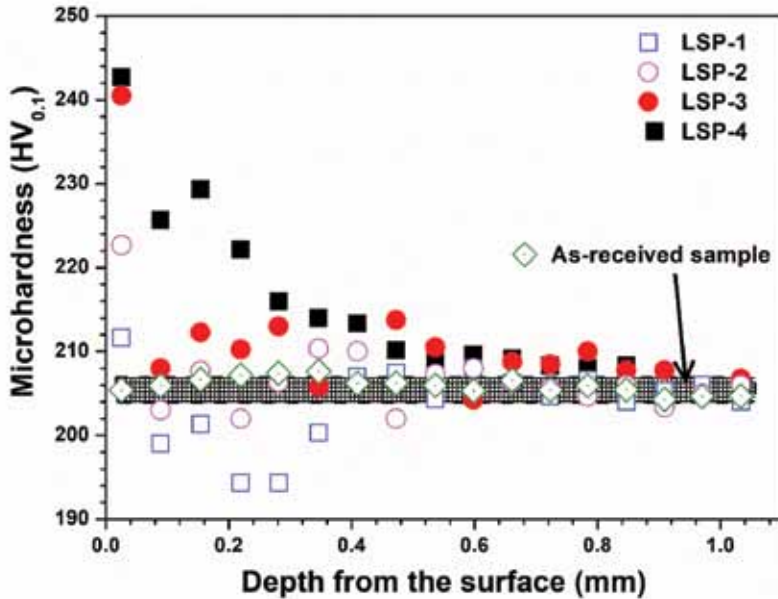


FIGURE 10

Microhardness distribution with depth in laser shock peened Hastelloy-X superalloy samples.

respectively as shown in Figure. 10. From Figure. 10, it is evident that the microhardness on the surface is higher than the interior with a gradual distribution of microhardness across its depth. From Figure. 10, the LSP surface treatment shows improved surface hardening as compared to an untreated sample. A maximum increment in hardness of $\sim 16.8\%$ was measured following LSP. Wang *et al* [20] found an increment in microhardness of 16.5% in K403 alloy following single-shot LSP which is close to what was measured in the present study. The depth of hardened zone is extended up to 500 mm which is greater than the value (300 mm) reported by Wang *et al* [20]. Hua *et al* [25] found an increment in microhardness of 27% and the depth of hardened zone was found to be 250 mm. A $\sim 20\%$ increase in the microhardness value and wide hardened zone of ~ 700 mm was reported by Gill *et al* [26]. A wider hardened zone may be obtained by multiple impacts at the same point during LSP. The gradual decrease in the microhardness values with depth is related to the decrease in the dislocation density with depth as shock pressure decreases as the shock waves travel from surface towards interior of the sample. The surface experiences a maximum shock pressure which goes on in a decreasing trend. The observed surface hardening phenomena is related to the increased dislocation density following LSP surface treatment (*cf.* Figure. 8). The enhanced surface hardening behavior of Hastelloy-X superalloys following LSP surface treatment would also improve the wear resistance of the

superalloy under study and should be a subject of future studies. It may be noted that there are some anomalies in the plot for LSP-2 and LSP-3 which indicates some additional mechanisms taking place here which is a subject for future study.

5 CONCLUSIONS

This investigation aims at studying the effectiveness of Laser Shock Peening (LSP) to tailor the surface properties of a new Hastelloy-X superalloys. This was done by focusing on understanding the evolution of phase, dislocation density, microstructure, surface hardening, and residual stress following LSP. A single-shot strategy was used to quantify depth of compressive residual stress following LSP. Microstructure and property analyses were undertaken to establish the mechanism of surface hardening. The investigation led to the following conclusions.

- (i) Microstructural refinement and reduction in grain size were observed with single-shot LSP. The measured grain sizes were between 23 nm to 30 nm. The single-shot LSP showed ~60% reduction in grain size as compared to the untreated sample.
- (ii) A maximum *rms* microstrain of 1.321×10^{-3} was measured on the surface of the Hastelloy-X. The *rms* microstrain increased with increase in the laser power density except for LSP-4 where confinement layer breakdown was believed to have occurred. Crystallite size showed a boost following LSP as compared to an untreated sample. With increase in laser power density, the crystallite size, respectively, showed a decreasing trend.
- (iii) Single-shot LSP showed increase in dislocation density. A maximum dislocation density of $26.3 \times 10^{13} \text{ m}^{-2}$ was measured for the laser power density of 14.1 GW/cm^2 . With increase in the laser power density, the dislocation density increased. However, the increment was within the same order of magnitude of untreated sample.
- (iv) Single-shot LSP induced a maximum compressive residual stress of 850 MPa when laser shock peened with a laser power density of 7.96 GW/cm^2 . On the other hand, a laser power density of 14.1 GW/cm^2 showed comparatively lower residual stress development which may be due to the confinement layer breakdown phenomena. In-depth residual stress measurement showed the depth and magnitude of compressively deformed zone varies with laser power density.
- (v) The surface hardening was achieved following LSP. A maximum surface hardness of 243 HV0.1 was measured following LSP. The increased hardness of the Hastelloy-X samples following LSP will increase the

strength and wear resistance and hence, it is expected to increase the component life and reduce the repair cost although further testing and analyses are necessary.

The enhanced hardness and significantly high compressive residual stress observed in the present study would significantly contribute to the application of Hastelloy-X in a gas turbine environment as well as in high temperature gas cooled reactors where cyclic loads are prevalent.

ACKNOWLEDGEMENT

The authors of this paper would like to thank EPSRC funded laser-loan-pool scheme for granting a state-of-the-art shock peening laser system (Grant no: EP/G03088X/1, (13250017 - NSL4)).

NOMENCLATURE

M^2	Beam quality factor
HEL	Hugoniot Elastic Limit (GPa)
P	Peak plasma pressure (GPa)
I_0	Laser power density (W/cm^2)
P_{avg}	Average laser power (W)
f	Pulse repetition rate (Hz)
Z	Reduced shock impedance ($gcm^{-2}s^{-1}$)
Z_1	Reduced shock impedance of nickel ($4.14 \times 10^6 gcm^{-2}s^{-1}$)
Z_2	Reduced shock impedance of water ($0.165 \times 10^6 gcm^{-2}s^{-1}$)
A	Laser spot area (cm^2)
E	Laser energy (J)
E_t	Total available energy (J)
K	Scherer constant (≈ 1)
D	Crystallite size or domain size (nm)
hkl	Indices of a crystallographic plane
σ	Lattice deformation stress (MPa)
b	Burger vector (nm)
a	Lattice parameter (nm)
S_{max}	Maximum residual stress (MPa)
S_{min}	Minimum residual stress (MPa)

Greek symbols

α	Efficiency of laser-material interaction (0.1 – 0.2)
τ	Laser pulse duration (ns)
ν	Poisson's ratio of the material.

σ_Y^{dyn}	Dynamic Yield strength (MPa)
β	Full width half maximum (Radian)
θ	X-ray diffraction angle ($^\circ$)
λ	X-ray wavelength (nm)
ε	Microstrain
ε^{hkl}	Microstrain in the <i>hkl</i> direction
$\langle \varepsilon^2 \rangle^{1/2}$	Root mean square microstrain
ρ	Dislocation density ($1/m^2$)

REFERENCES

- [1] Sakthivel T., Laha K., Nandagopal M., Chandravathi K.S., Parameswaran P., Selvi S.P., Mathew M.D. and Mannan, S.K. Effect of temperature and strain rate on serrated flow behaviour of Hastelloy X. *Material Science and Engineering A* **534** (2012), 580-587.
- [2] Kim W.G., Yin S.N., Ryu W.S. Chang J.H. and Kim S.J. Tension and creep design stresses of the “Hastelloy-X” alloy for high-temperature gas cooled reactors. *Material Science and Engineering A* **483/484** (2008), 495-497.
- [3] Lee J.W. and Kuo Y.C. A study on the microstructure and cyclic oxidation behavior of the pack aluminized Hastelloy X at 1100 $^\circ$ C. *Surface and Coatings Technology* **201** (2006), 3867-3871.
- [4] Mizokami Y., Igari T., Kawashima F., Sakakibara N., Tanihira M., Yuhara T. and Hiroe T. Development of structural design procedure of plate-fin heat exchanger for HTGR. *Nuclear Engineering Design* **255** (2013), 248-262.
- [5] Cho H., Lee D.M., Lee J.H., Bang K.H. and Lee B.W. Thermal oxidation behavior of ceramic-coated Ni–Cr-base superalloys. *Surface and Coatings Technology* **202** (2008), 5625-5628
- [6] Ding K. and Ye L. *Laser Shock Peening Performance and Process Simulation*. Cambridge: Woodhead Publishing. 2006.
- [7] Peyre P. and Fabbro R. Laser shock processing: a review of the physics and applications. *Optical and Quantum Electronics* **27** (1995), 1213-1229.
- [8] Peyre P., Fabbro R., Merrien P. and Lieurade H.P. Laser shock processing of aluminium alloys. Application to high cycle fatigue behaviour. *Material Science and Engineering A* **210** (1996), 102-113.
- [9] Lu J.Z., Qi H., Luo K.Y., Luo M. and Cheng X.N. Corrosion behaviour of aisi 304 stainless steel subjected to massive laser shock peening impacts with different pulse energies. *Corrosion Science* **80** (2014), 53–59.
- [10] Lim H., Kim P., Jeong H. and Jeong S. Enhancement of abrasion and corrosion resistance of duplex stainless steel by laser shock peening. *Journal of Materials Processing Technology* **212** (2012), 1347– 1354.
- [11] Montross C.S., Wei T., Ye L., Clark G. and Mai Y.W. Laser shock processing and its effects on microstructure and properties of metal alloys: A review. *International Journal of Fatigue* **24** (2002), 1021–1036.
- [12] Rubio-González C., Felix-Martinez C., Gomez-Rosas G., Ocana J.L. Morales M., and Porro J.A. Effect of laser shock processing on fatigue crack growth of duplex stainless steel. *Material Science and Engineering A* **528** (2011), 914–919.
- [13] Shukla P., Nath S., Wang W., Shen X. and Lawrence J. Surface property modifications of silicon carbide ceramic following laser shock peening. *Journal of the European Ceramic Society* **37** (2017), 3027-3038.
- [14] Shukla P., Robertson S., Wu H., Telang A., Kattoura M., Nath S., Mannava S.R., Vasudevan V.K. and Lawrence J. Surface engineering alumina armour ceramics with laser shock peening. *Materials Design* **134** (2017), 523-538.

- [15] Kashaev N., Ventzke V., Horstmann M., Chupakhin S., Riekehr S., Falck R., Maawad E., Staron P., Schell N. and Huber N. Effects of laser shock peening on the microstructure and fatigue crack propagation behaviour of thin AA2024 specimens. *International Journal of Fatigue* **98** (2017), 223-233.
- [16] Salimianrizi A., Foroozmehr E., Badrossamay M. and Farrokhpour H. Effect of laser shock peening on surface properties and residual stress of Al6061-T6. *Optics and Lasers in Engineering* **77** (2016), 112-117.
- [17] Luo K.Y., Lin T., Dai F.Z., Luo X.M. and Lu J.Z. Effects of overlapping rate on the uniformities of surface profile of LY2 Al alloy during massive laser shock peening impacts. *Surface and Coatings Technology* **266** (2015), 49-56.
- [18] Trdan U. and Grum J. SEM/EDS Characterization of laser shock peening effect on localized corrosion of Al alloy in a near natural chloride environment. *Corrosion Science* **82** (2014), 328-338.
- [19] Trdan U., Skarba M. and Grum J. Laser shock peening effect on the dislocation transitions and grain refinement of Al-Mg-Si alloy. *Materials Characterization* **97** (2014), 57-68.
- [20] Wang C., Shen X.J., An Z.B., Zhou L.C. and Chai, Y. Effects of laser shock processing on microstructure and mechanical properties of K403 nickel-alloy. *Materials & Design* **89** (2016), 582-588.
- [21] Gill A.S., Telang A. and Vasudevan V.K. Characteristics of surface layers formed on Inconel 718 by laser shock peening with and without a protective coating. *Journal of Materials Processing Technology* **225** (2015), 463-472.
- [22] Lu G.X., Liu J.D., Qiao H.C., Zhou Y.Z., Jin T., Zhao J.B., Su X.F. and Hu Z.Q. Surface nano-hardness and microstructure of a single crystal nickel base superalloy after laser shock peening. *Optics and Lasers in Engineering* **91** (2017), 116-119.
- [23] Amini S., Dadkhah M. and Teimouri R. Study on laser shock peening of Incoloy 800 super alloy. *Optik* **140** (2017), 308-316.
- [24] Kattoura M., Mannava S.R., Qian D. and Vasudevan V.K. Effect of laser shock peening on residual stress, microstructure and fatigue behavior of ATI 718Plus alloy. *International Journal of Fatigue* **102** (2017), 121-134.
- [25] Hua Y., Rong Z., Ye Y., Chen K., Chen R., Xue Q. and Liu H. Laser shock processing effects on isothermal oxidation resistance of GH586 superalloy. *Applied Surface Science* **330** (2015), 439-444.
- [26] Gill A., Telang A., Mannava S.R., Qian D., Pyoun Y.S., Soyama H., Vasudevan V.K. Comparison of mechanisms of advanced mechanical surface treatments in nickel-based superalloy. *Material Science and Engineering A* **576** (2013), 346-355.
- [27] Forget P., Jeandin M. and Lyoret A. Determination of laser shock treatment conditions for fatigue testing of Ni-based superalloys. *Journal de Physique IV* **3** (1993), 921-926.
- [28] Zhou W.F., Ren X.D., Ren Y.P., Xu S.D., Huang J.J. and Yang T. Laser shock processing on Ni-based superalloy K417 and its effect on thermal relaxation of residual stress. *The International Journal of Advanced Manufacturing Technology* **88** (2017), 675-681.
- [29] Li Y., Zhou L., He W., He G., Wang X., Nie X., Wang B., Luo S. and Li Y. The strengthening mechanism of a nickel-based alloy after laser shock processing at high temperatures. *Science and Technology of Advanced Materials* **14** (2013), 055010-055019.
- [30] Kumar D., Akhtar S.N., Patel A.K., Ramkumar J. and Balani K. Tribological performance of laser peened Ti-6Al-4V. *Wear* **322/323** (2015), 203-217.
- [31] Hongchao Q. Experimental investigation of laser peening on Ti17 titanium alloy for rotor blade applications. *Applied Surface Science* **351** (2015), 524-530.
- [32] Hongchao Q., Jibin Z., Gongxuan Z. and Yu G. Effects of laser shock peening on microstructure and residual stress evolution in Ti-45Al-2Cr-2Nb-0.2B alloy. *Surface and Coatings Technology* **276** (2015), 145-151.
- [33] Zhou Z., Bhamare S., Ramakrishnan G., Mannava S.R., Langer K., Wen Y., Qian D., Vasudevan V.K. Thermal relaxation of residual stress in laser shock peened Ti-6Al-4V alloy. *Surface and Coatings Technology* **206** (2012), 4619-4627.

- [34] Cellard C., Reirant D., François M., Rouhaud E. and Le Saunier D. Laser shock peening of Ti-17 titanium alloy: Influence of process parameters. *Material Science and Engineering A* **532** (2012), 362-372.
- [35] Shen X., Shukla P., Nath S., Lawrence J. Improvement in mechanical properties of titanium alloy (Ti-6Al-7Nb) subject to multiple laser shock peening. *Surface and Coatings Technology* **327** (2017), 101-109.
- [36] Yella P., Venkateswarlu P., Buddu R.K., Vidyasagar D.V., Sankara Rao K.B., Kiran P.P. and Rajulapati K.V. Laser shock peening studies on SS316LN plate with various sacrificial layers. *Applied Surface Science* **435** (2018), 271-280.
- [37] Hoppius J.S., Kukreja L.M., Knyazeva M., Pöhl. F. Walther F., Ostendorf A. and Gurevich, E.L. On femtosecond laser shock peening of stainless steel AISI 316. *Applied Surface Science* **435** (2018), 1120-1124.
- [38] Zheng L., Zhang C., Zhang C., Dai F. Performance of micro-dent array fabricated by laser shock peening on the surface of A304 stainless steel. *Vacuum* **138** (2017), 93-100.
- [39] Spadaro L., Gomez-Rosas G., Rubio-González C., Bolmaro R., Chavez-Chavez A. and Hereñú S. Fatigue behavior of superferritic stainless steel laser shock treated without protective coating. *Optics and Lasers in Engineering* **93** (2017), 208-215.
- [40] Halilović M., Issa S., Wallin M., Hallberg H. and Ristinmaa M. Prediction of the Residual State in 304 Austenitic Steel after Laser Shock Peening – Effects of Plastic Deformation and Martensitic Phase Transformation. *International Journal of Mechanical Sciences* **111/112** (2016), 24-34.
- [41] Ge M., Xiang J., Fan Z., Lu Y.L. and Lei W.N. Effect of laser energy on microstructure of Mg-3Al-1Zn alloy treated by LSP. *Journal of Alloys and Compounds* **734** (2018), 266-274.
- [42] Ren X.D., Huang J.J., Zhou W.F., Xu S.D., Liu F.F. Surface nano-crystallization of az91d magnesium alloy induced by laser shock processing. *Materials & Design* **86** (2015), 421-426.
- [43] Liu L., Wang J. and Zhou J. Effects of laser shock peening on mechanical behaviors and microstructural evolution of brass. *Vacuum* **148** (2018), 178-183.
- [44] Trdan U. and Grum J. Evaluation of corrosion resistance of AA6082-T651 aluminium alloy after laser shock peening by means of cyclic polarisation and EIS methods. *Corrosion Science* **59** (2012), 324-333.
- [45] Abotula S., Shukla A. and Chona R. Dynamic constitutive behavior of Hastelloy X under thermo-mechanical loads. *Journal of Material Science* **46** (2011), 4971-4979.
- [46] Shukla P.P., Lawrence J. The influence of brightness whilst laser surface processing of a silicon nitride engineering ceramic. *Optics and Lasers in Engineering* **50** (2012), 1746-17512.
- [47] Shukla P.P. and Lawrence J. Role of laser beam radiance in different ceramic processing: a two wavelength comparison. *Optics and Lasers in Engineering* **54** (2013), 380 – 388.
- [48] Shukla P., Lawrence J. and Zhang Yu. Understanding laser-beam brightness: a review on a new prospective in materials processing. *Optics and Lasers in Engineering* **75** (2015), 40 – 51.
- [49] Shukla P.P. and Lawrence J. Identification of optical parameters for determination of radiance. *Journal of Optics* **44** (2015), 12-19
- [50] Fabbro R., Fournier J., Ballard P., Devaux D. and Virmont J. Physical study of laser-produced plasma in confined geometry. *Journal of Applied Physics* **68** (1990), 775-784.
- [51] Suryanarayana C. and Norton M.G. *X-Ray Diffraction: A Practical Approach*. New York: Springer 1998.
- [52] Khorsand Zak A., Majid W.H.Abd., Abrishami M.E. and Yousefi R. X-Ray analysis of zno nanoparticles by Williamson–Hall and size–strain plot methods. *Solid State Science* **13** (2011), 251-256.
- [53] Williamson G.K. and Smallman R.E. Dislocation densities in some annealed and cold worked metals from measurements on the X-ray Debye-Scherrer spectrum. *Philosophical Magazine* **1** (1956), 34-46.

- [54] Shadangi Y., Chattopadhyay K., Rai S.B. and Singh V. Effect of LASER shock peening on microstructure, mechanical properties and corrosion behavior of interstitial free steel. *Surface and Coatings Technology* **280** (2015), 216–224.
- [55] Gujba A.K. and Medraj M. Laser peening process and its impact on materials properties in comparison with shot peening and ultrasonic impact peening. *Materials* **7** (2014), 7925-7974.
- [56] Fairand B.P. and Clauerthe A.H. Effect of water and paint coatings on magnitude of laser-generated shocks. *Optics Communication* **18** (1976), 588-591.
- [57] Hong X., Wang S., Guo D., Wu H., Wang J., Dai Y., Xia X. and Xie Y. Confining medium and absorptive overlay: their effects on a laser-induced shock wave. *Optics and Lasers in Engineering* **29** (1998), 447-455.